Title

On Electrical Current in Nanostructured Electrochemical Cells

Author

Yamada, Hidenori

Publication Date

2018

UNIVERSITY OF CALIFORNIA SAN DIEGO

On Electrical Current in Nanostructured Electrochemical Cells

A dissertation submitted in partial satisfaction of the requirements for the degree Doctor of

Philosophy

in

Electrical Engineering (Applied Physics)

by

Hidenori Yamada

Committee in charge:

Professor Prabhakar R. Bandaru, Chair
Professor Peter M. Asbeck, Co-Chair
Professor Clifford P. Kubiak
Professor Yuan Taur
Professor Paul K. Yu

2019

The Dissertation of Hidenori Yamada is approved, and it is acceptable in quality and form for publication on microfilm and electronically:

Co-Chair

Chair

University of California San Diego

2019

TABLE OF CONTENTS

LIST OF FIGURES

ACKNOWLEDGEMENTS

To Prof. Bandaru, Prof. Asbeck, and my father for many fruitful discussions, and to my friends and family for all the support.

Chapter 1, in full, is a reprint of the material as it appears in H. Yamada, P.R. Bandaru, Applied Physics Letters **102**, 173113 (2013). The dissertation author was the primary investigator and author of this paper.

Chapter 2, in full, is a reprint of the material as it appears in H. Yamada, P.R. Bandaru, Appl. Phys. Lett. **104**, 213901 (2014). The dissertation author was the primary investigator and author of this paper.

Chapter 3, in full, is a reprint of the material as it appears in H. Yamada, P.R. Bandaru, AIP Adv. **6**, 065325 (2016). The dissertation author was the primary investigator and author of this paper.

Chapter 4, in full, is a reprint of the material as it appears in H. Yamada, R. Narayanan, P. R. Bandaru, Chem. Phys. Lett. **695**, 24-27 (2018). The dissertation author was the primary investigator and author of this paper.

Chapter 5, in full, is a reprint of the material as it appears in R. Narayanan, H. Yamada, M. Karakaya, R. Podila, A. M. Rao, and P. R. Bandaru, Nano Lett. **15**, 3067-3072 (2015). The dissertation author was a co-author of this paper, and handled all of the theory and simulations.

Chapter 6, in full, is a reprint of the material as it appears in R. Narayanan, H. Yamada, B. C. Marin, A. Zaretski, and P. R. Bandaru, J. Phys. Chem. Lett. **8**, 4004-4008 (2017). The dissertation author was a co-author of this paper, and handled all of the theory and simulations.

VITA

2010 Bachelor of Science, University of California Berkeley

2012 Master of Science, University of California San Diego

2019 Doctor of Philosophy, University of California San Diego

PUBLICATIONS

H. Yamada, R. Narayanan, P. R. Bandaru, “Electron Tunneling in Nanoscale Electrodes for Battery Applications”, Chem. Phys. Lett. **695**, 24 (2018).

H. Yamada, P. R. Bandaru, “Electrochemical kinetics and dimensional considerations, at the nanoscale”, AIP Adv. **6**, 065325 (2016).

H. Yamada, P. R. Bandaru, “Enhanced electrical current densities in electrochemical systems through the use of nanostructured electrodes”, App. Phys. Lett. **104**, 213901 (2014).

H. Yamada, P. R. Bandaru, “Limits to the magnitude of capacitance in carbon nanotube array electrode based electrochemical capacitors”, App. Phys. Lett., **102** 173113-1 (2013).

R. Narayanan, H. Yamada, B. C. Marin, A. Zaretski, and P. R. Bandaru, “Dimensionality-Dependent Electrochemical Kinetics at the Single-Layer Graphene–Electrolyte Interface”, J. Phys. Chem. Lett. **8**, 4004 (2017).

R. Narayanan, H. Yamada, M. Karakaya, R. Podila, A. M. Rao, and P. R. Bandaru, “Modulation of the Electrostatic and Quantum Capacitances of Few Layered Graphenes through Plasma Processing”, Nano Letters **15(5)**, 3067 (2015).

ABSTRACT OF THE DISSERTATION

On Electrical Current in Nanostructured Electrochemical Cells

by

Hidenori Yamada

Doctor of Philosophy in Electrical Engineering (Applied Physics)

University of California San Diego, 2019

Professor Prabhakar R. Bandaru, Chair

Professor Peter M. Asbeck, Co-Chair

An electrochemical cell is an energy storage device that involves both electrons and ions as part of the storage mechanism. In this work, we investigate the use of nanostructures on the electrodes of the cell to increase the active surface area, and the consequent quantum effects introduced to the cell. With regards to capacitive storage, we predict quantum capacitance will affect the storage capacity of electrons on the electrode, and limit the increase in total capacitance of the device from scaling with the increase in active surface area. Furthermore, we predict geometric effects will affect the screening ability of ions in the electrolyte, allowing device current during charge/discharge cycles to be higher than for a flat electrode. With regards to battery-like storage, we predict the density of states of the electrode will affect the device current, possibly increasing device currents for higher overpotentials compared to a flat electrode battery. This last

prediction is based on treatment of the redox reaction process as a tunneling process between electron and ion, akin to a recombination process between electron and hole in a solid state device such as a reverse biased diode.

INTRODUCTION

In this work, I analyze the inner workings of an electrochemical cell through principles of electron transport from solid state physics, adapted to both electrons in solid and ions in liquid. These same principles were used by Shockley and Bardeen to make sense of the point-contact transistor and began an entire industry based on the design of more optimized transistors such as the bipolar junction transistor and the field effect transistor. My goal with this work is to make the design principles of the electrochemical cell more accessible to the scientific community. This goes beyond empirical fitting, instead assigning elements of solid state physics (density of states), device physics (energy band diagrams), electromagnetism (screening), statistical physics (Fermi-Dirac & Boltzmann distribution), and quantum physics (electron transport) to the cell. As a result, this work required a deep understanding of both applied physics and electron devices, an approach distinct from the standard approach in electrochemistry. I developed a methodology by drawing heavy inspiration from Shockley and Bardeen and adapting it to a solid-to-liquid interface by treating ions as vehicles for electrons. My hope is that this treatment becomes a successful integration of electrochemistry, solid state physics, device physics, and electromagnetism, and that I was able to take the first step towards this ambitious view. I believe this approach results in research with high originality, and would like to continue this style throughout my professional career.

1. Limits to the magnitude of capacitance in carbon nanotube array electrode based electrochemical capacitors

Electrochemical energy storage may be broadly classified as encompassing either batteries or electrochemical capacitors (ECs). While the former category incorporates devices with high energy density (~ 100 Wh/kg) and relatively low power density (~ 1 kW/kg), the latter comprises media with opposite attributes, *i.e.,* relatively lower energy density (~ 10 Wh/kg) and higher power density (~10 kW/kg)[1,2]. The overarching imperative is then to devise *intermediate* ECs, combining the best of both energy and power densities. Moreover, characteristics such as a high cycle life, *i.e.* the capability of rapid charging and discharging, for millions of cycles must be incorporated.

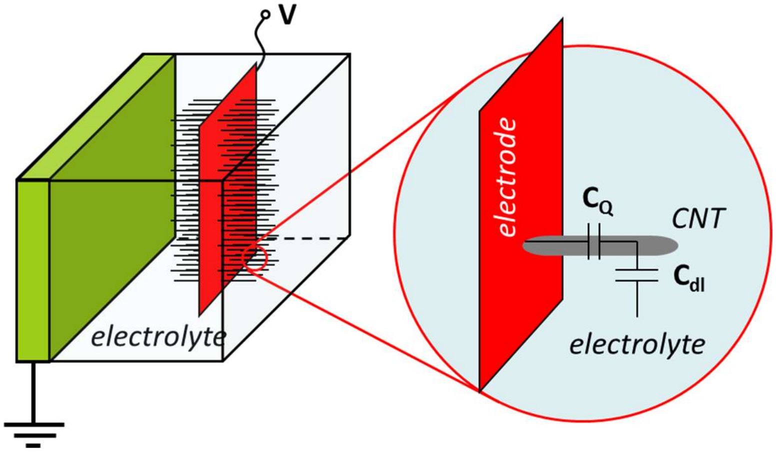

Figure 1-1. A schematic of electrode configuration in an electrochemical capacitor, zoomed into a section of the CNT array. C_Q and C_{dl} in series represented within a single CNT. As the surface area for the CNT electrode (in red) is much higher than that of the counter electrode (in green), the capacitance of the former is much more significant.

Much EC work has focused on charge storage in a *double layer* comprised of the electrode charge and electrolyte charge of opposite polarity – Figure 1. The double layer capacitance/unit area (C_{dl}) is directly proportional to the dielectric constant ($\varepsilon = \varepsilon_o \varepsilon_r$, where ε_o is the permittivity of free space and is equal to $8.854 \cdot 10^{-12}$ F/m and ε_r is the relative permittivity, *e.g.,* ~ 80 for water) and inversely proportional to the charge separation distance between the positive (+) and negative (-) charges. C_{dl} is further constituted of a *Helmholtz* capacitance, where distances are of the order of the electrolyte ionic diameters, as well as a *diffusive* capacitance, with mean distances of the order of the Debye length[3] ($d = \sqrt{\frac{\varepsilon k_B T}{2N_A (ze)^2 I}} \sim 9.78 \frac{1}{\sqrt{I}}$ nm) where k_B ($=1.38 \cdot 10^{-23}$ J/K) is the Boltzmann constant, T is the absolute temperature (K), N_A ($= 6.02 \cdot 10^{23}$ atoms/mole) is the Avogadro number, (ze) is the net charge with e as the elementary electronic charge ($=1.6 \cdot 10^{-19}$ C), and I (in moles/m^3) is the electrolyte concentration. For an aqueous electrolyte (@ 1 M concentration), C_{dl} could then *potentially* be of the order of 250 μF/cm^2. The utilization of a high surface area electrode substrate, *e.g.,* carbon nanotubes (CNTs), where the total surface area would be much larger[4] than the projected area would also be beneficial. However, the values reported in literature are typically an order of magnitude lower[5], and this has been tentatively ascribed to incomplete/inadequate utilization of the surface area[6]. A substantial addition to the total capacitance (C_{tot}) through the utilization of *parallel* redox capacitance/pseudocapacitance (C_p), which mimics battery like behavior[7], could also be obtained in ECs as discussed in a previous study[8,9]. It was found that ion irradiation, facilitated through plasma processing, increased the observed C_{tot}. However, details of the underlying mechanisms were not specified. In this article, we propose a possible mechanism through detailed comparison with experiment and seek to understand the limits of capacitance that may be manifested with a given CNT configuration. The underlying principles may be adapted to other nanostructure and device types as well.

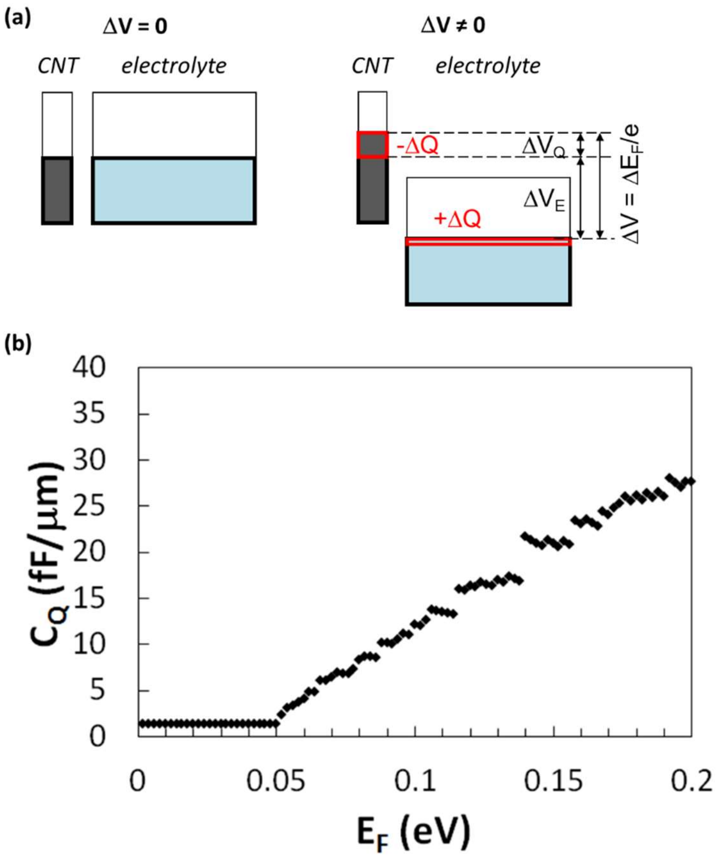

Figure 1-2. **(a)** Representation of CNT DoS and electrolyte DoS (as columns) along with their respective Fermi energies (E_F) at equilibrium, with no applied voltage ($\Delta V = 0$) - *top figure,* and with a non-zero applied voltage ($\Delta V \neq 0$) - *bottom figure*. The *applied* ΔV causes a differential change in the E_F (of ΔE_F) and is partitioned between the CNT electrode (as ΔV_Q) and the bulk electrolyte (ΔV_E). While ΔV_Q would be associated with the C_Q, the ΔV_E is related to the C_{dl}. **(b)** The quantum capacitance (C_Q) as a function of E_F in a MWCNT with 15 walls. The initially flat C_Q is caused by the metallic CNT walls. The staircase like structure arises from the contributions of successive sub-bands to the DoS.

We considered quantum capacitance (C_Q), which is relevant when nanostructures such as CNTs, with a finite density of states (DoS) $D(E)$, as depicted in Figure 2. The increase (/decrease) of the Fermi energy (E_F) of the CNTs could be significant, relative to the bulk electrolyte, when charge carriers of a single type, *e.g.,* electrons of magnitude dQ ($= e \cdot dn$), are added (/removed) due to an applied voltage change (dV)[10]. An effective capacitance could therefore be defined for a given electrode, considering the DoS at the E_F, as follows:

$$C_Q = \frac{dQ}{dV} = \frac{edn}{\frac{1}{e}dE_F} = e^2 D(E_F) \quad . \tag{1}$$

We model the *net* device capacitance in Figure 1 as a series combination of C_{dl} *and* C_Q. If, as hypothesized[8,11], the role of ion irradiation (*e.g.,* through plasma processing) was to introduce fixed charges, then C_Q increases significantly with increasing processing time. The series combination of C_Q and C_{dl} would allow an increase in C_{tot} consistent with the experiment as can be understood through:

$$\frac{1}{C_{tot}} = \frac{1}{C_{dl}} + \frac{1}{C_Q} \quad . \tag{2}$$

It should be pointed out that our work focuses on correlating the capacitance contributions from MWNTs (with concentric nanotubes of gradually decreasing perimeters) while previous works, *e.g.,* by Fang, *et al*[12] and Xia, *et al*[13], are on graphene sheets or nanoribbons, the latter of which have sub-bands due to the finite width and become graphene sheets in the infinite width limit. The C_Q of for nanoribbons and graphene was discussed in Ref. 12 for MOSFET (metal oxide semiconductor field effect transistor)-like devices. While they discussed the series addition of the gate oxide capacitance and the C_Q, we discuss the series addition of the double layer capacitance (C_{dl}) with the C_Q, as appropriate for an electrochemical capacitor. The maximum carrier concentration (n) studied in Ref. 12 was less than $2\cdot 10^{12/}\text{cm}^2$ with concomitant C_Q values of the order of 10 μF/cm^{2,} which seem to be comparable with the values calculated in this article. In Ref. 13, they fabricated experimental MOSFET-like devices using a graphene sheet and analyzed their data. Accordingly, there was no need to consider sub-band contributions, but for our purposes, counting contributions of several tens of all relevant sub-bands is critical and that is what will be performed below.

We modeled multi-walled CNT (MWCNT) characteristics, in accordance with previous experiments which used such ensembles (with average individual MWCNT diameter of 20 nm and spacing 200 nm on a 5 mm × 5 mm Si substrates) as electrodes[8,11]. We calculated the DoS of a constituent wall in a MWCNT, following previous methodology[10,14], modeled as a rolled graphene sheet (infinite in the *y*-direction and both periodic and finite in the orthogonal *x*-direction). It was assumed that the walls are independent of each other[15], with the implication that the total DoS can be obtained as the sum of the DoS for each constituent wall. We considered zigzag CNTs (involving rolling of the graphene sheet in the *x*- direction), as this category encompasses both semiconducting and metallic CNTs[16]. As we consider relatively large diameter CNTs[11], the details as to how graphene is rolled to yield CNTs, *i.e.,* whether zigzag or armchair or chiral[17], will not influence the C_Q. The exact dispersion relation for a graphene sheet, through the tight-binding approximation[10,18] is

$$E\left(k_x, k_y\right) = \pm\gamma_1\sqrt{1 + 4\cos\left(\frac{\sqrt{3}ak_y}{2}\right)\cos\left(\frac{ak_x}{2}\right) + 4\cos^2\left(\frac{ak_x}{2}\right)} \quad . \tag{3}$$

In (3), $a = \sqrt{3}\,a_0$ where a_0 (= 0.142 nm) is the C- C bond length and the overlap integral γ_1 = 2.9 eV[15]. The 20 nm MWCNT with 15 walls was *approximately* indexed through [*N, 0*] (with $N = 250$ for the outermost wall and decreasing by 10 for each successive inner wall) and was effectively one dimensional since $k_{x,n} = \frac{2q\pi}{Na}$ (*q*: sub-band index), while k_y is continuous. The DoS for a single sub-band is then $\frac{4}{2\pi}\frac{dk_y}{dE}$ with k_{xn} held constant, and the 4 in the numerator accounted for the electron spin degeneracy and the positive/negative k_y.

Since C_Q is a function of E_F from (1), we needed to estimate an appropriate value for E_F. In a graphene sheet *with no impurities*, each carbon atom provides one electron to the p_z orbital, yielding semi-metallic behavior and implying[19] an $E_F = 0$ eV, and zero carrier density (n) at $T = 0$ K. However, n could range around $4.6 \cdot 10^{12}$ cm^{-2}, corresponding to the two-dimensional carrier density interpolated from the experimental value for bulk graphite[1] of 10^{19} cm^{-3}, *i.e.,* through $(10^{19})^{2/3}$. With variability in n, *e.g.,* due to defects[13], *etc.,* attempting an exact E_F would yield imprecise values, and it could then be appropriate to estimate n by approximating the CNTs as sheets of graphene and calculating the DoS, as was done here. The n of $4.6 \cdot 10^{12}$/cm^2 is then only posited as a representative number for the purpose of illustrating the concepts. The actual n in any sample could either be below *or* above[20] this number with a corresponding decrease/increase in the C_Q.

From the total carrier concentration at the Fermi energy, $n(E_F) = \int_0^\infty D(E) f(E) dE$. The $f(E)$ is the Fermi-Dirac function and was approximated as a step function in our calculations, as the difference between the value of $f(E)$ with a finite temperature (T=300 K) and with $T = 0$ K was at most 5 %. The E_F values were found to range around 278 meV (with $n = 4.6 \cdot 10^{12}$ cm^{-2}). Computing $E_F(k_{x,n}, k_y)$ from (3), and then $C_Q(k_{x,n}, k_y)$ from (1), pairs of E_F and C_Q for all sub-bands $k_{x,n}$ over the Brillouin zone for k_y are plotted in Figure 2 (b). $C_Q(E_F)$ is constant initially due to the metallic CNTs, up to ~ $E_F = 50$ meV, due to the constituent metallic NTs with finite and constant DoS, where C_Q does not increase as there is no sub-band contribution from the NTs. The staircase like structure in the variation results from the contribution of successive sub-bands to the DoS. At

E_F = 278 meV we estimate, in units of capacitance per NT length, C_Q = 48 fF/μm. The linearity in the plot justifies starting with the graphene E_F-k relation to estimate the E_F of the CNT from n. We next consider the two major components, which add in series, of the C_{dl}: (i) a *Helmholtz* capacitance (C_H) due to a Coulombic attraction, and (ii) a *Gouy-Chapman* (C_{GC}) capacitance due to the diffusive distribution of ions in the electrolyte[3]. An area average C_H can be computed from a spatial separation corresponding to the ionic radius[11] (*e.g.,* r ~ 0.278 nm for K^+ ions in $K_3Fe(CN)_6$) and is equal to ε/r. The C_{GC} is estimated from the voltage drop (ϕ) across the diffusive region (which is of the order of the Debye length, d) and is equal to $(\varepsilon/d)\ \cosh\ (e\phi/2k_BT)$. Consequently,

$$\frac{1}{C_{dl}} = \frac{r}{\varepsilon} + \frac{d}{\varepsilon}\frac{1}{\cosh\left(\dfrac{e\phi}{2k_BT}\right)} \quad . \tag{4}$$

At smaller ϕ (→ 0) the $C_{dl} \rightarrow C_{GC}$, at ϕ (~ $3k_BT$) the C_H and C_G are comparable, and at a larger ϕ (> $10k_BT$), the $C_{dl} \rightarrow C_H$. With a range of ϕ from zero to 278 mV (corresponding to the E_F), we estimate from (4), a range of C_{dl} for an electrolyte concentration, I (in moles/m^3), from ~ $7.3\sqrt{I}$ μF/cm^2 to ~ 255 μF/cm^2. In order to compare to the one-dimensional quantum capacitance C_Q estimated above, we convert the units of C_{dl} by multiplying by $2\pi r$, where r = 10 nm is the outer MWCNT wall radius. The corresponding range is then from $4.6\sqrt{I}$ fF/μm to 160 fF/μm. For a given I, say 3 mM as in the experiments (see Table V of Ref. 11), the C_{dl} is calculated to be 7.9 fF/μm. With C_Q = 48 fF/μm, this results in a C_{tot} ~6.8 fF/μm. Generally, the electrostatic interaction between surfaces of different geometries decays with a characteristic decay length equal to the Debye length[21]. Equivalent capacitances are then obtained for the planar/cylindrical cases.

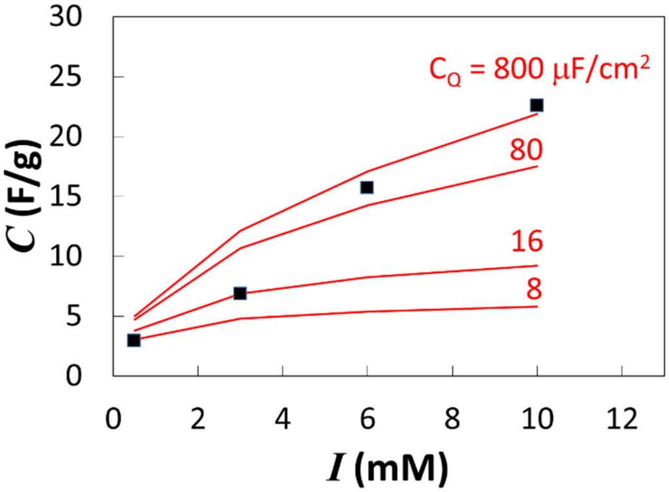

Figure 1-3. Comparison of experimentally measured capacitance (see Ref. 11) in ■ with numerical estimates (red lines) of C_Q, as a function of electrolyte concentration, I. A value of $C_Q = 80$ μF/cm^2 corresponds to the theoretically predicted $C_Q = 48$ fF/μm. The match is strongest for low I with low C_Q and for high I with high C_Q.

The capacitance per projected electrode area is the product of the obtained C_{tot}, the average CNT length, L (= 100 μm), the estimated CNT density on the substrate, λ (~ $2.5\cdot10^9$ cm^{-2}), and the projected surface area of the electrode, A (~ 0.25 cm^2) yielding an expected capacitance value per projected area of ~ 1700 μF/cm^2. Dividing this value by the weight of the CNTs (~ 40 μg), the capacitance values, in F/g, were computed and are shown in comparison to the experimental values (details have been previously reported[8,11]) in Figure 3. The figure then indicates the relative magnitudes of C_Q relevant to the measured capacitances and indicates a variable C_Q, being more significant (for a series combination of C_{dl} and C_Q) at lower electrolyte concentrations when the CNT is sufficiently isolated so that its DoS is small. We generally observe from the figure that while higher electrolyte concentrations may be adequately modeled through the use of C_{dl} alone, lower concentrations need C_Q as well. C_Q is significant when the CNT is sufficiently isolated so that its DoS is small. As I increases, charge transfer between CNT and electrolyte may be more likely, reducing isolation and increasing the CNT DoS effectively so that C_Q increases and becomes insignificant, as per equation (2).

Several insights are obtained through our analyses. For example, the magnitudes of both C_Q and C_{dl} are comparable and suggest an explanation for the considerable (up to 300 %) increase in C_{tot} when the CNT constituted electrodes are subject to argon plasma processing[8,11]. Such exposure was hypothesized to introduce charged acceptor like defects into the NT's carbon lattice, through argon abstracting electronic charge from the carbon bonds. Much like surface states in semiconductors[22], the fixed charges in the CNT lattice are immobile, and do not respond to applied voltage and would not contribute directly to the C_{dl}. However, the added charge density (which would be proportional to the exposure time) affects the Fermi energy and enhances C_Q. A higher C_Q closer to C_{dl} enhances the maximum C_{tot} that could be obtained from a given system. We can also conclude that the limits to the magnitude of the capacitance that can be obtained from CNT or nanostructure based electrochemical capacitors is a function of the series combination of *both* the electrostatic/double layer capacitance as well as the quantum capacitance. In a situation where both are comparable, one would need to increase the C_Q, say through varying the charge density and maximize the total capacitance.

Acknowledgments

This work was supported by the US National Science Foundation under grant ECS-0643761. The authors thank Professor P. M. Asbeck for useful discussions, as well as Dr. M. Hoefer and Professor P. Yu for relevant comments.

Chapter 1, in full, is a reprint of the material as it appears in H. Yamada, P.R. Bandaru, Applied Physics Letters **102**, 173113 (2013). The dissertation author was the primary investigator and author of this paper.

References

[1] J. R. Miller and A. F. Burke, The Electrochemical Society Interface**, 17,** 53-57 (2008).

[2] J. M. Miller, *Ultracapacitor Applications* (The Institution of Engineering and Technology, Herts, UK, 2011).

[3] A. J. Bard and L. R. Faulkner, *Electrochemical Methods: Fundamentals and Applications*, 2 ed. (John Wiley, New York, 2001).

[4] A. Peigney, C. Laurent, E. Flahaut, R. R. Basca, and A. Rousset, Carbon **39,** 507-514 (2001).

[5] P. Simon and Y. Gogotsi, Nature Materials **7,** 845-854 (2008).

[6] L. R. Radovic, in *Carbons for electrochemical energy storage and conversion systems*, edited by F. Beguin and E. Frackowiak (CRC Press, New York, 2010).

[7] B. E. Conway, Journal of the Electrochemical Society **138,** 1539-1548 (1991).

[8] M. Hoefer and P. R. Bandaru, Applied Physics Letters **95,** 183108 (2009).

[9] J. A. Nichols, H. Saito, M. Hoefer, and P. R. Bandaru, Electrochemical and Solid State Letters **11,** K35-K39 (2008).

[10] S. Datta, *Quantum Transport: Atom to Transistor* (Cambridge University Press, New York, 2005).

[11] M. Hoefer and P. R. Bandaru, Journal of Applied Physics **108,** 034308 (2010).

[12] T. Fang, A. Konar, H. Xing, and D. Jena, Applied Physics Letters **91,** 092109 (2007).

[13] J. Xia, F. Chen, J. Li, and N. Tao, Nature Nanotechnology **4,** 505-509 (2009).

[14] L. Forro and C. Schonenberger, in *Carbon Nanotubes- Topics in Applied Physics*; *Vol. 80*, edited by M. S. Dresselhaus, G. Dresselhaus, and P. Avouris (Springer-Verlag, Heidelberg, 2001).

[15] R. Saito, G. Dresselhaus, and M. S. Dresselhaus, Physical Review B **61,** 2981-2990 (2000).

[16] P. R. Bandaru, Journal of Nanoscience and Nanotechnology **7,** 1239-1267 (2007).

[17] R. Saito, M. Fujita, G. Dresselhaus, and M. S. Dresselhaus, Applied Physics Letters **60,** 2204-2206 (1992).

[18] C. Beenakker, Reviews of Modern Physics **80,** 1337-1354 (2008).

[19] M. I. Kastnelson, *Graphene: Carbon in Two Dimensions* (Cambridge University press, Cambridge, UK, 2012).

[20] D. K. Efetov and P. Kim, Physical Review Letters **105,** 256805 (2010).

[21] J. N. Israelachvili, *Intermolecular and Surface Forces,*, 3 ed. (Academic Press, San Diego, 2011).

[22] J. Bardeen, Physical Review **71,** 717-727 (1947).

2. Enhanced electrical current densities in electrochemical systems through the use of nanostructured electrodes

An important problem in modern day science and technology, related to energy capacity, concerns both increasing the amount of stored electrical charge as well as enhancing the rate at which the charge could be taken up or released. In this regard, fuel cells or batteries[2] have been acknowledged to be prototypes for high energy concomitant with low power capabilities, brought about by charge storage in the bulk and diffusion related limitations, respectively. Alternately, electrical capacitors have contrary attributes, *i.e.,* through being recognized as low energy and high power devices, mediated through the charge being located at/close to the surface. It then seems to be clear that obtaining both high energy and power could be facilitated through electrochemical reactions that are not diffusion limited. As diffusion is essentially a bulk or volume based phenomena[3], alternate mechanisms for charge storage mainly operate through increasing the effective surface area, *e.g.,* through either enhancing the number of charge storage sites on the surface[4], or through using thin layer electrochemical models[5] where all the charge is stored in the intervening electrolyte between closely spaced structures and diffusion is unnecessary for reactions on the surface.

It is then understood that the essential elements underlying charge storage and transfer involve the interaction of ions in the electrolyte with the electrode through either diffusion to the surface and subsequent electrochemical reaction or the latter alone (as in the thin layer case), under the influences of forces[6] due to a concentration gradient or electric field, respectively. In this paper, we seek to re-examine the fundamentals of charge transfer in terms of electric field induced ion drift from the bulk of the electrolyte. We intend to show that such drift currents would dominate the diffusion currents in the bulk. The resulting new equation is consistent with the conventional equation derived from the completely different regime of diffusion current at the electrode surface. In comparison to experiment, we find that the drift-based equation can explain a broader spectrum of data.

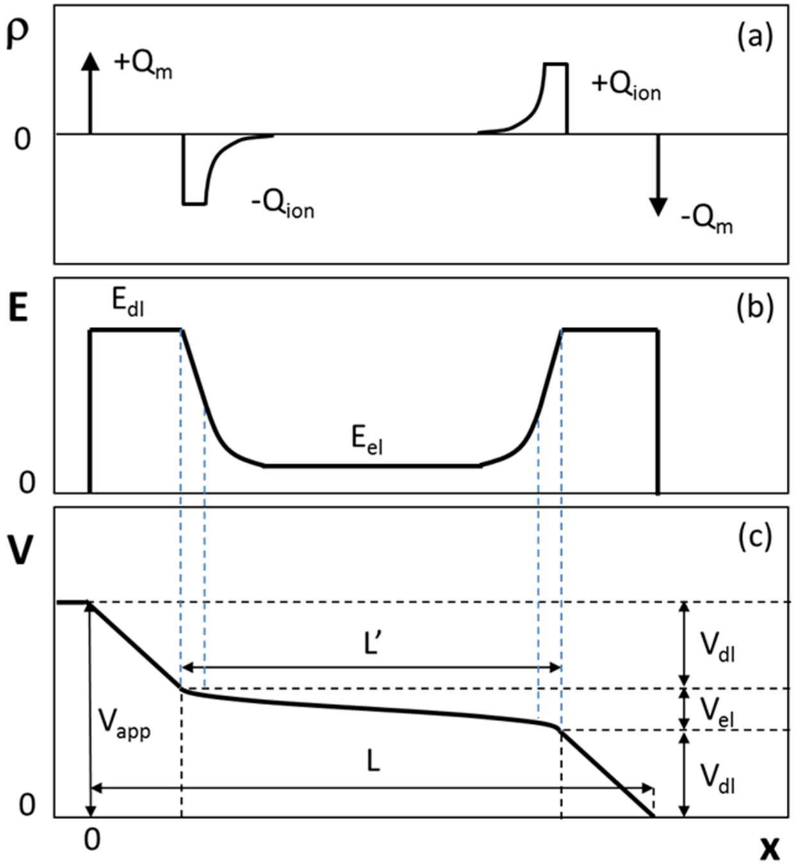

Figure 2-1. **(a)** Schematic representation of the charge density ρ, with electrode charge Q_m and electrolyte ion Q_{ion}. L is the total device length. **(b)** The electric field E, with double-layer field E_{dl} and electrolyte field E_{el}. E is symmetric, and L' is the length excluding the double-layers. **(c)** The electric potential V, with double-layer potential $2V_{dl}$ and electrolyte potential V_{el}. The counter electrode is assigned a reference potential of zero.

We consider an electrode with a net charge density per unit volume Q_m in contact with an electrolyte of total charge density Q_{ion}, as in **Figure 1(a).** While the formation of an electrical double layer[5] on the surface of an electrode, due to charge compensation or screening from the electrolyte, is reasonably well understood, the spatial distribution of the ions may be complex. We examine a simplified version where the ions do not perfectly screen the electrode charge, *i.e.* $Q_{ion} < Q_m$, and a one-dimensional charge variation. We assign the spacing between the electrodes to be L, and that between the edges of the double layers to be L', implying that the thickness of the double layer t_{dl} on an electrode would be, on average, equal to $(L - L')/2$ where $2t_{dl} << L$.

The variation in electric field E in the device ($0 < x < L$) in both the double layer E_{dl} and the electrolyte E_{el}, as in **Figure 1(b),** can be obtained from $E = \int_0^x \frac{\rho}{\varepsilon} dx$, with ρ as the respective charge density (= Q_m or Q_{ion}) and ε being the equivalent and uniform dielectric permittivity[7]. When Q_{ion} is only slightly smaller than Q_m, E_{dl} would be significantly larger than E_{el}. Further spatial integration leads to the potential profile $V(x) = -\int_L^x E\, dx$, with the potential of the counter electrode set to a reference value of zero as in **Figure 1(c)**. Consistent with $E_{dl} > E_{el}$, the voltage across the double layer V_{dl} would be significantly larger than that across the electrolyte V_{el}. It is to be noted that the applied voltage across the electrodes/device is $V_{app} = 2V_{dl} + V_{el}$.

As the charge distribution in the double layer is related to the electrolyte ion radius and to thermal fluctuations, it occurs over spatial scales typically several orders of magnitude smaller than the device length, so there is no appreciable difference between representing the double layer to be of a finite width vs. that of a sharply peaked distribution for the purposes of partitioning V_{app}. Nonetheless, the shape of Q_{ion} in **Figure 1(a)** reflects the fixed electrical double layer closer to the electrode – reckoned with respect to the outer Helmholtz plane, and the adjacent diffuse double layer with an exponential decay in the ion concentration[5].

We define γ as a measure of the screening strength[8] of the electrode charge through

$$\gamma = \frac{V_{el}}{V_{app}} \quad . \tag{1}$$

Considering that $V_{app} \approx 2t_{dl}E_{dl} + L'E_{el}$, $V_{el} \approx L'E_{el}$, $E_{dl} = Q_m/\varepsilon$, and $E_{el} = (Q_m - Q_{ion})/\varepsilon$, we can also derive

$$\frac{Q_{ion}}{Q_m} = 1 - \frac{2t_{dl}}{L'}\frac{\gamma}{1-\gamma} \quad . \tag{2}$$

In this form, with $\gamma = 0$, $Q_{ion}/Q_m = 1$, meaning that the double layer holds exactly as much charge as the electrode and we have perfect screening; there would no driving force for an electrochemical redox (reduction-oxidation) reaction in this case. With $\gamma = L'/L$, $Q_{ion}/Q_m = 0$, meaning that there is no screening whatsoever of the electric field from the double-layer to the bulk electrolyte. Note that γ cannot be equal to 1 in this formulation.

We now study the behavior of ions in the electrolyte under the influence of E_{el}, which induces a drift velocity $\dot{x} = \mu E_{el}$, with μ being the ion mobility. Then the electrical current density is $J = q(CN_A)\dot{x}$ with $q = ne$, where n is the charge per ion, e is the elementary electronic charge, C is the bulk electrolyte molar concentration, and N_A is the Avogadro constant. We regard a typical experiment in electrochemistry, *e.g.,* cyclic voltammetry (CV) which can determine the complete electrochemical behavior of a system[5] and is often used to monitor the nature and reversibility of the cathodic and anodic reactions in an electrolyte[9,10]. CV involves a linear sweep of V_{app}, recording the net electrical current through the electrodes. The rate of change of the voltage, known as the scan rate $\nu = dV_{app}/dt$, can be related to E_{el} using Eqn. (1) by

$$E_{el} = \frac{dV_{el}}{dx} = \frac{d(\gamma V_{app})}{dx} = \gamma \frac{dV_{app}/dt}{dx/dt} = \frac{\gamma \nu}{\dot{x}} \quad . \tag{3}$$

It is assumed that γ is spatially independent, since neither V_{el} nor V_{dl} are spatially dependent. Then, $\dot{x} = \mu E_{el} = \mu \frac{\gamma \nu}{\dot{x}}$ so that $\dot{x} = \sqrt{\gamma \mu \nu}$. This new $\dot{x}$ is converted into J through $J = q(CN_A)\dot{x}$. Further bookkeeping through the Einstein relation $\mu = \frac{qD}{k_B T}$ and the equality $\frac{F}{RT} = \frac{e}{k_B T} = \frac{q/n}{k_B T}$, where D is the diffusion coefficient, k_B is the Boltzmann constant, T is the temperature, F is the Faraday constant, and R is the gas constant, yields

$$J = \sqrt{\gamma} \cdot C \sqrt{F^3 \frac{D\nu}{RT}} n^{\frac{3}{2}} \quad . \tag{4}$$

Such a form for the current density has been previously established through invoking elaborate semi-infinite diffusion based techniques and cited in literature[5,11,12] as the Randles-Seŝvcik (R-S) equation $J = a \cdot C \sqrt{F^3 \frac{D\nu}{RT}} n^{\frac{3}{2}}$ with a being a numerical constant. This equation is defined by mapping the redox reaction current to a diffusion current anchored to the electrode surface. The device operates in a closed circuit, so the currents thus defined at one surface are related to the currents at the opposing surface. It is possible to find an analytical integral equation for device current as a function of time $i(t)$, after which the normalized current may be numerically plotted as a function of t. The normalized peak current[5] is $a = 0.4463$; the corresponding peak current density is hereby defined as J_{peak}. Therefore, there is no empirical parameter involved in a.

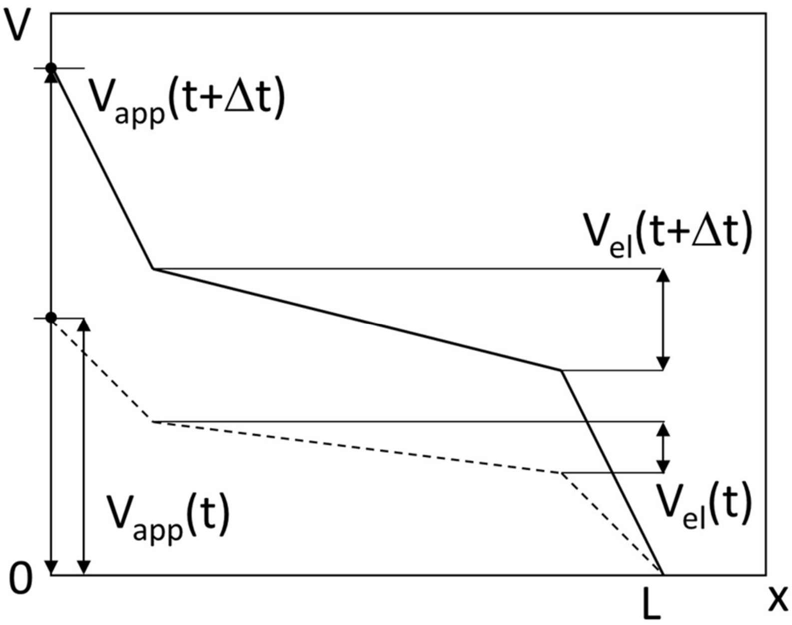

Figure 2-2. Comparing voltage profiles at times t and $t + \Delta t$, the increase in V_{app} is always greater than that for V_{el}. In general, a faster scan rate ν allows for a larger value of γ and thus V_{el} due to weaker screening.

We have now shown that electric field induced drift in the bulk electrolyte could yield a similar form for J, reinforcing the deep connection between drift and diffusion. Assuming an equivalence of our derived relation Eqn. (4) with the R-S equation, we can now assign a physical significance for the constant a,

$$\sqrt{\gamma} \text{ (proposed drift model)} = a \text{ (R-S equation)} \ . \qquad (5)$$

For example, a match of the R-S equation's a coefficient in J_{peak} of 0.4463 with $\sqrt{\gamma}$ leads to $\gamma \sim$ 0.2. In general, a larger value of γ corresponds to a larger value of V_{el}, though it is limited by V_{app}

as in **Figure 2.** Equivalently, J increases if screening can be weakened without affecting the other factors in Eqn. (4).

The imperfect screening of Q_m by Q_{ion} causes V_{el} to be a fraction of V_{app}. At larger ν, the screening is further weakened since the ions cannot respond to the quicker change in V_{app}, resulting in a larger value of E_{el} and a larger ionic current density. Generally, the electric field induced drift current density J_{drift} may be assumed to be dominant over the diffusion current density J_{diff} from the bulk electrolyte, *i.e.* outside the double layer. This can be understood by taking the ratio of $J_{drift} = q(CN_A)\mu \frac{dV_{el}}{dx} \approx q(CN_A)\mu \frac{\gamma V_{app}}{L'}$ to $J_{diff} = qD\frac{d(CN_A)}{dx} \approx q\frac{k_B T}{q}\mu \frac{CN_A}{L'}$, which is equal to $\gamma \frac{V_{app}}{k_B T/q}$. At $T = 300$ K, by assuming a typical experimental input of $V_{app} = 1$ V, $k_B T/q \sim 26/n$ mV, so we have $J_{drift}/J_{diff} \sim 40\gamma/n$. For such electrolytes as $K_3Fe(CN)_6$, $n = 1$ for the positive ions and 3 for the negative ions. If $\gamma \sim 0.25$, as indicated and also justified later in the paper, then $J_{drift}/J_{diff} = 10/n >> 1$. As a result, for the assumed bias conditions, basing the total current on drift current is appropriate. The above formulations and conclusions apply to both positive and negative ions, albeit with different μ and n.

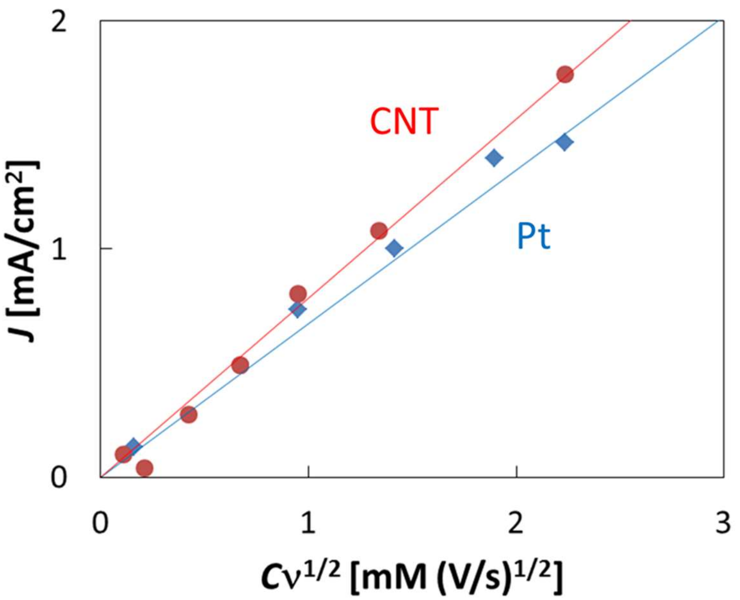

Figure 2-3. Current density J as a function of the product of the $K_3Fe(CN)_6$ molar concentration C and the square root of scan rate $\sqrt{\nu}$. Data from Ref. 8 by Hoefer and Bandaru. Flat Pt and nanostructured carbon nanotube (CNT) electrode data are compared to the drift model in Eqn. (4).

Comparison of our drift model to experimental current densities was used for additional insight into the nature and variation of γ. J vs. $C\sqrt{\nu}$ is plotted from experimental data for both flat Pt electrodes and for nanostructured CNT electrodes in **Figure 3**. Empirically, $J = 0.674\ C\sqrt{\nu}$ for Pt and $J = 0.786\ C\sqrt{\nu}$ for CNT. Assuming the same diffusion coefficient $D = 6.8 \times 10^{-6}$ cm^2/s for both positive and negative ions[5] and using $F = 96487$ C/mol, $R = 8.31$ J/mol · K, and $T = 300$ K, from Eqn. (4) we have $\sqrt{F^3 \frac{D}{RT}} = 1.56 \left[\frac{\text{mA/cm}^2}{\text{mM}\sqrt{\text{V/s}}}\right]$. Therefore, $J = \sqrt{\gamma}\ 1.56\ C\sqrt{\nu}$ for both Pt and CNT. For Pt, $\sqrt{\gamma} \sim 0.4327$ and thus $\gamma \sim 0.2$, in close accord to the theoretical R-S value of $a = 0.4463$ as in Eqn. (5). However, for CNT, $\sqrt{\gamma} \sim 0.5045$ and thus $\gamma \sim 0.25$. The experimental procedures as well as the relevant parameters and data for the fitting were taken from papers by

Hoefer, *et al*[4,13]. The precision to four significant figures is in keeping with the coefficient of the R-S equation. The CNT electrode consists of CNTs with average length, diameter, and separation[4] of 25 ± 4 μm, 20 ± 5 nm and 150 ± 50 nm.

A greater value of $\gamma \sim 0.25$ for CNT compared $\gamma \sim 0.2$ for Pt indicates that the screening of the electrode has been weakened, allowing a larger electric field in the electrolyte. The consequent larger magnitude of E_{el} and J_{drift} could account for the larger current densities of **Figure 3** for the nanostructured electrodes. It is to be noted from the figure suggests that the slopes of the current (*I)* – concentration-scan rate product ($C\sqrt{\nu}$) *might be* different for two experiments, *i.e.,* for Pt electrodes computed using the traditional models and for CNT electrodes analyzed through the newer formulation. The close spacing of the CNTs could result in a relative starvation of the screening ions from the electrolyte yielding a greater value of γ, and suggests design methodologies to further increase electrical current densities.

In summary, we have indicated the principles through which the net current density of electrochemical devices can be analyzed by ionic drift current from the bulk electrolyte. A metric γ, related to the ratio of the potential drop in the electrolyte to that of the applied voltage, has been introduced through which the current density increase, in terms of $\sqrt{\gamma}$, may be parameterized. A preliminary comparison between flat electrodes and nanostructured electrodes seems to indicate larger current densities for the latter, which can be explained more readily through $\sqrt{\gamma}$. However, reduced electric field screening is fundamental to the improved electrical current densities and there is no obvious relation to the micro-/nano-structure of the electrode. Further optimization electrochemical devices considering such principles and based on the fact that the theoretical upper limit for $\sqrt{\gamma}$ approaches 1, would be worthy of continued study.

Acknowledgements

We acknowledge the financial support (through CMMI 1246800) of the National Science Foundation (NSF). Discussions with Professor Peter Asbeck of the Department of Electrical and Computer Engineering at UC San Diego and R. Narayanan are deeply appreciated.

Chapter 2, in full, is a reprint of the material as it appears in H. Yamada, P.R. Bandaru, Appl. Phys. Lett. **104**, 213901 (2014). The dissertation author was the primary investigator and author of this paper.

References

[1] C. Klein and W. Straub, Phys. Rev. **123**, 1581 (1961).

[2] D. Linden and T.B. Reddy, *Linden's Handbook of Batteries* (McGraw Hill, New York, NY, 2010).

[3] S.J. Konopka and B. McDuffie, Anal. Chem. **42**, 1741 (1970).

[4] M. Hoefer and P.R. Bandaru, J. Electrochem. Soc. **160**, H360 (2013).

[5] A.J. Bard and L.R. Faulkner, *Electrochemical Methods: Fundamentals and Applications*, 2nd ed. (John Wiley, New York, 2001).

[6] H.B. Callen, *Thermodynamics* (John Wiley Inc., New York, 1960).

[7] R.S. Muller, T.I. Kamins, and M. Chan, *Device Electronics for Integrated Circuits*, 3rd ed. (John Wiley and Sons, New York, 2003).

[8] N.W. Ashcroft and N.D. Mermin, *Solid State Physics* (Saunders College, Orlando, FL, 1976).

[9] M. Hoefer and P.R. Bandaru, Appl. Phys. Lett. **95**, 183108 (2009).

[10] R.G. Compton and C.E. Banks, *Understanding Voltammetry* (Imperial College Press, London, UK, 2011).

[11] C.M.A. Brett and A.M.O. Brett, *Electrochemistry: Principles, Methods, and Applications* (Oxford University Press, Oxford, 1993).

[12] P.H. Rieger, *Electrochemistry*, 2nd ed. (Chapman and Hall, New York, 1994).

[13] M. Hoefer and P.R. Bandaru, J. Appl. Phys. **108**, 34308 (2010).

[14] Kuznetrsov, *Charge Transfer in Physics, Chemistry and Biology: Physical Mechanisms of Elementary Processes and an Introduction to the Theory* (CRC Press, 1995).

[15] J.-M. Savéant, *Elements of Molecular and Biomolecular Electrochemistry: An Electrochemical Approach to Electron Transfer Chemistry* (John Wiley & Sons, Inc., New York, NY, 2006).

[16] H. Yamada and P.R. Bandaru, Appl. Phys. Lett. **102**, 173113 (2013).

[17] H. Yamada and P.R. Bandaru, Appl. Phys. Lett. **104**, 213901 (2014).

[18] R.A. Marcus, J. Chem. Phys. **24**, 966 (1956).

[19] N. Sutin, J. Phys. Chem. **90**, 3465 (1986).

[20] N.S. Hush, J. Electroanal. Chem. **470**, 170 (1999).

[21] M.C. Henstridge, E. Laborda, N. V. Rees, and R.G. Compton, Electrochim. Acta **84**, 12 (2012).

[22] C.E. Chidsey, Science **251**, 919 (1991).

[23] R.A. Marcus, J. Electroanal. Chem. (2000).

[24] T.M. Cover and J.A. Thomas, *Elements of Information Theory* (Wiley-Interscience, Hoboken, NJ, 2006).

[25] G. Grampp, Angew. Chemie Intl. Edn. **32**, 691 (1993).

[26] J.R. Miller, L.T. Calcaterra, and G.L. Closs, J. Am. Chem. Soc. **106**, 3047 (1984).

[27] T.T.T. Li and M.J. Weaver, J. Am. Chem. Soc. **106**, 6107 (1984).

[28] S. Datta, *Quantum Transport: Atom to Transistor* (Cambridge University Press, New York, 2005).

[29] P. Bai and M.Z. Bazant, Nat. Commun. **5**, 3585 (2014).

[30] J.R. Miller, J. V. Beitz, and R.K. Huddleston, J. Am. Chem. Soc. **106**, 5057 (1984).

[31] J. V. Beitz and J.R. Miller, J. Chem. Phys. **71**, 4579 (1979).

[32] R. Narayanan, H. Yamada, M. Karakaya, R. Podila, A.M. Rao, and P.R. Bandaru, Nano Lett. **15**, 3067 (2015).

[33] M.I. Kastnelson, *Graphene: Carbon in Two Dimensions* (Cambridge University press, Cambridge, UK, 2012).

[34] S. Das Sharma, S. Adam, E.H. Hwang, and E. Rossi, Rev. Mod. Phys. **83**, 407 (2011).

[35] P.R. Bandaru, J. Nanosci. Nanotechnol. **7**, 1239 (2007).

[36] S. Fletcher, J. Solid State Electrochem. **14**, 705 (2010).

[37] P.R. Bandaru, H. Yamada, R. Narayanan, and M. Hoefer, Mater. Sci. Eng. R Reports **96**, 1 (2015).

[38] H. Gerischer, in *CRC Handb. Solid State Electrochem.*, edited by P.J. Gellings and H.J.M. Bouwmeester (CRC Press, Boca Raton, FL, 1997).

[39] A.J. Bard and L.R. Faulkner, *Electrochemical Methods: Fundamentals and Applications*, 2nd ed. (Wiley, Hoboken, 2001).

[40] R. Narayanan, H. Yamada, B.C. Marin, A. Zaretski, and P.R. Bandaru, J. Phys. Chem. Lett. **8**, 4004 (2017).

[41] H. Yamada and P.R. Bandaru, AIP Adv. **6**, 65325 (2016).

[42] R.A. Marcus, Rev. Mod. Phys. **65**, 599 (1993).

[43] N.S. Hush, J. Chem. Phys. **28**, 962 (1958).

[44] H. Yamada and P.R. Bandaru, (2017).

[45] R.S. Muller and T.I. Kamins, *Device Electronics for Integrated Circuits* (Wiley, New York, 1977).

[46] J.R. Schrieffer, Rev. Mod. Phys. **36**, 200 (1964).

[47] J. Bardeen, Phys. Rev. Lett. **6**, 57 (1961).

[48] J. Bardeen, Phys. Rev. Lett. **9**, 147 (1962).

[49] G. Binnig, H. Rohrer, C. Gerber, and E. Weibel, Phys. Rev. Lett. **49**, 57 (1982).

[50] G. Binnig, C.F. Quate, and C. Gerber, Phys. Rev. Lett. **56**, 930 (1986).

[51] W.A. Harrison, Phys. Rev. **123**, 85 (1961).

[52] J.B. Goodenough and Y. Kim, Chem. Mater. **22**, 587 (2010).

[53] W. Zhu, T. Low, V. Perebeinos, A.A. Bol, Y. Zhu, H. Yan, J. Tersoff, and P. Avouris, Nano Lett. **12**, 3431 (2012).

[54] V.M. Pereira, A.H. Castro Neto, H.Y. Liang, and L. Mahadevan, Phys. Rev. Lett. **105**, 156603 (2010).

[55] M. Gilbertini, A. Tomadin, F. Guinea, M.I. Kastnelson, and M. Polini, Phys. Rev. B **85**, 201405(R) (2012).

[56] J. Martin, N. Akerman, G. Ulbricht, T. Lohmann, J.H. Smet, K. von Klitzing, and A. Yacoby,

Nat. Phys. **4**, 144 (2008).

[57] N.L. Ritzert, J. Rodríguez-López, C. Tan, and H.D. Abruña, Langmuir **29**, 1683 (2013).

[58] M.C. Henstridge, C. Batchelor-McAuley, R. Gusmão, and R.G. Compton, Chem. Phys. Lett. **517**, 108 (2011).

3. Electrochemical kinetics and dimensional considerations, at the nanoscale

A critical understanding of the thermodynamics and kinetics inherent to electrochemical reactions is necessary for scientific insights into charge transfer[14] as well as in applications ranging from biochemical reactions[15] to charge storage in capacitors[16,17] and batteries[2]. While the foundational attributes have almost always been reckoned in terms of one-electron based charge transfer[5,10], much of the theoretical and experimental analysis has only obliquely referred to the considerations of dimensionality. Consequently, three-dimensional electrode characteristics and classical thermodynamics have been implicitly assumed in heterogeneous electron transfer kinetics, encompassing the widely used Butler-Volmer (BV) formulations and the subsequent Marcus[18,19] – Hush[20] interpretations. In this regard, Arrhenius based activation theory, leading to the BV approaches, has been used for over a century, and extensively documented in standard electrochemistry textbooks[5,12]. In the BV case, the rate constant (K^{BV}), considering that for the forward reaction rate (K_F) and for the backward reaction (K_B), is

$$K^{BV} = K_F + K_B = K^o exp\left[\frac{\alpha e\eta}{k_B T}\right] + K^o exp\left[-\frac{(1-\alpha)e\eta}{k_B T}\right] \ . \qquad (1)$$

In Eqn. (1), α is the electron transfer coefficient and η refers to the overpotential (= V - V^o), with V as the applied voltage and V^o as the standard redox potential. e is the elementary unit of electronic charge, k_B is the Boltzmann constant, and T is the temperature. While simple to use, in principle, such an approach does not yield substantial insight into the type and involvement of the specific constituents (redox species as well as the electrode) and α is phenomenologically determined. The

Marcus-Hush (MH) theory then seeks to better understand the rationale for K^o and α through a more detailed consideration[21] of the reorganization dynamics of the solvent and the redox species *vis-à-vis* the electrochemical reactions and the electrolyte (through the macroscopic dielectric constant).

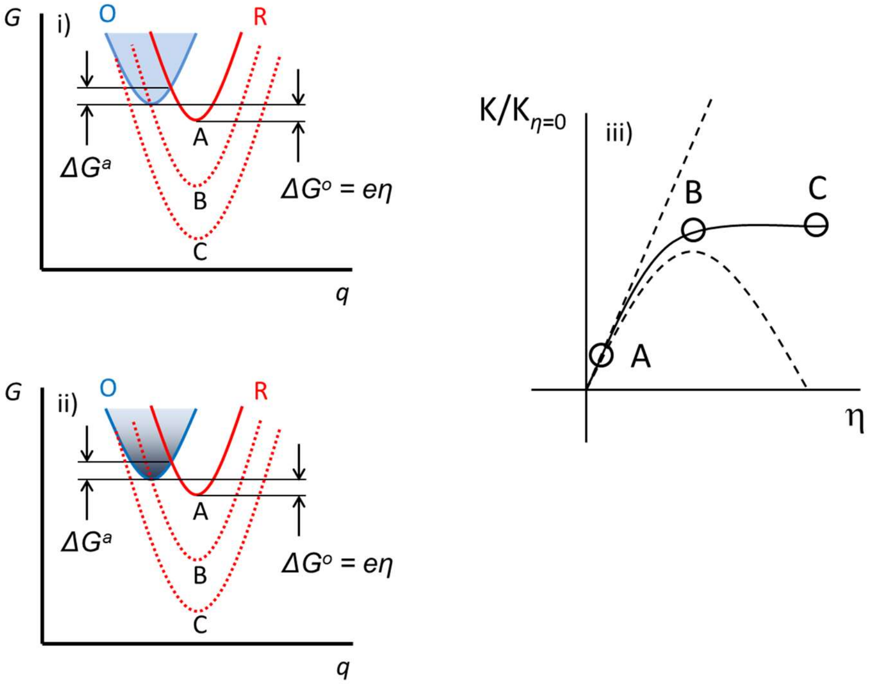

Figure 3-1. **(a)** Gibbs free energy (G) - reaction coordinate (q) curves for the oxidized (O) and reduced (R) species in an electrochemical redox reaction, of the type: $O + e^- \rightleftharpoons R$. The free energy of reaction (ΔG^o), and the free energy of activation (ΔG^a) are indicated, for several applied voltages (η) and resulting R species configurations. **(b)** For low-dimensional structures, variation in the density of states (*DOS*) accessible for electron transfer, as in the lowering of the *DOS* for a one-dimensional system, would yield equivalent behavior. **(c)** The operating points corresponding to the various R curves in (i) and (ii) represented in the normalized rate constant ($K/K_{\eta=0}$)-η plot.

We first briefly review the salient features of the MH kinetics approach and its extension by Chidsey[22]. Consequently, we consider typical[18,19] Gibbs free energy (G) – reaction coordinate (q) curves: Fig. 1. Typically, the reaction coordinate has been broadly interpreted[23], and may refer to the distance[24], in a multi-dimensional *extensive* variable sense (*e.g.,* the change of bond length, electrical charge, *etc.*), between the oxidized (O) and reduced (R) species in an electrochemical redox reaction, of the type: $O + e^- \rightleftharpoons R$. While the progressive lowering of the minimum energy of the R parabola (*e.g.,* through increasing the η) always decreases the free energy of reaction ΔG^o, the *free energy of activation* ΔG^a initially decreases, reaching zero when the R parabola passes through the minimum of the O parabola, and subsequently increases, due to a shift of the R free energy curves to the left hand side of the O parabola: Fig. 1(a). The concomitant increase and decrease of the electrochemical reaction rate constant K^{MH}, *i.e.,* as represented in Eqn. (2), with v as the attempt frequency, reaches a maximum when $\Delta G^a = 0$.

$$K^{MH} = vexp\left[-\frac{\Delta G_a}{k_B T}\right] = vexp\left[-\frac{(\lambda \mp e\eta)^2}{4\lambda k_B T}\right] \quad . \tag{2}$$

Such a non-intuitive increase and subsequent decrease of the reaction rate with increasing driving force (*i.e.,* η) constitutes the essence of the *inverted region,* particular to the Marcus-Hush theory. Such a notion on the maximum of a rate constant has been experimentally confirmed[25], *e.g.,* in intramolecular reactions, concerning molecules with bridged donor – acceptor units[26]. It may also be derived that [25], $\Delta G^a = \frac{\lambda}{4}\left(1+\frac{\Delta G^o}{\lambda}\right)^2$, with λ as the reorganization energy - which is related to the energy required for both the internal (*e.g.,* due to the bond configuration changes) and the external (*e.g.,* in the rearrangement of the solvation shell, surrounding electrolyte, *etc.*) configurational changes. Subsequently, it is evident that a zero ΔG^a would imply that the peak of the K^{MH} is at a value of $\lambda \sim -\Delta G^o$.

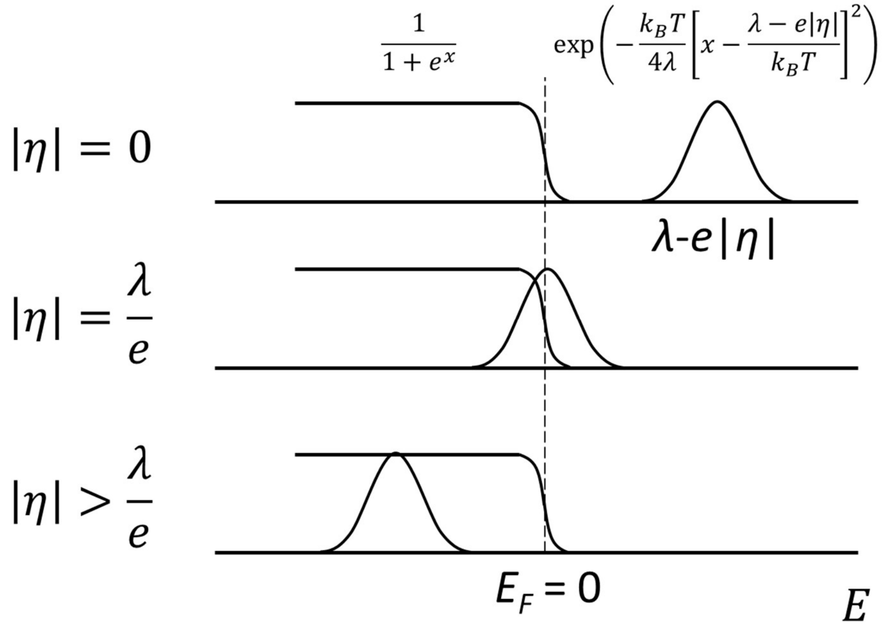

Figure 3-2. The Chidsey formulation for the rate constant in Eqn. (3) can be interpreted as indicating the relative overlap between the Fermi-Dirac distribution function f_{FD} (E) – on the *left*, and the Gaussian curve – on the *right*, corresponding to the MH models. The *DOS* was considered to be constant. In the figure, x = $(E-E_F)/k_BT$, λ is the reorganization energy and η is the overpotential.

However, such a theory seemed to be incompatible with the notion of long distance interfacial electron transfer where the rate constant decreases exponentially with increased donor-acceptor separation distances [27] as considered through the seminal work of Chidsey[22]. Additionally, the experimental observation, in certain metal electrode based electrochemical ensembles of the saturation of the electrochemical current with increasing η, prompted the consideration of a continuum of energy level states. The consequently derived rate constant K^{MHC}, considering energy level occupancy through the Fermi-Dirac distribution f_{FD}, and the explicit introduction of a constant metallic electronic density of states (*DOS*) (= ρ), was of the form[22]

$$K^{MHC} = v(\rho k_B T) \int_{-\infty}^{\infty} \frac{1}{1+\exp(x)} exp\left(-\frac{k_BT}{4\lambda}\left[x - \frac{\lambda \mp e\eta}{k_BT}\right]^2\right) dx \qquad (3)$$

The variable $x = \dfrac{E - E_F}{k_B T}$ refers to the normalized energy of a relevant participating level (E), *e.g.,* in the electrode, relative to the Fermi energy (E_F) and the negative sign is used for $\eta > 0$. The integration limits may be narrowed down to either the negative interval (-∞, 0] or the positive interval [0, ∞), if f_{FD} (E) can be approximated by a step function, which would be applicable when η exceeds 26 mV ($=k_BT/e$). The MHC relation, indicated in Eqn. (3), may also be interpreted as related to the area of overlap between the f_{FD} and an Arrhenius based rate law: Fig. 2. This figure indicates that at low η, BV theory may be adequate to model the electrochemical kinetics while increasing η leads to overlap and the Chidsey extension. However, at $|\eta| = \lambda/e$ and beyond, the electrical current starts to decrease, and saturation may be expected when $|\eta|$ is significantly larger compared to the λ/e. The constant height of the step function results from an assumption of a constant *DOS*.

The MHC relation seems to yield excellent agreement with the experimental observation of the rate constant, which tends to a constant value at larger electrode overpotential. It is to be noted that the rate constants, *e.g.,* the K^{MHC} are typically obtained through chronoamperometry (CA) experiments, through the electrical current I decay with time t (in response to a step-voltage change) of the form: $I=I_o \exp(-K^{MHC}t)$. However, even in such molecular systems, the Chidsey modification to the Marcus-Hush theory adopts an intrinsically continuum point of view, through assuming a constant ρ.

In this paper, through considering the DOS of the electrode to be a distribution over energy instead of a constant value, we broadly aim to extend the utility of the Marcus-Hush-Chidsey (MHC) kinetics to a larger class of materials and situations. While constant *DOS* can explain K-η trends for macroscale electrodes, the limited carrier density for nanoscale electrodes causes unexpected behavior for *K* at higher values of η. For instance, we observe in zero-dimensional (0-D) or one-dimensional (1-D) nanostructured electrodes, electrical current oscillations as a function of the η, corresponding to the gradual population (and de-population) of each successive sub-band. We posit that the consideration of a variable/non-constant *DOS* leads to a deeper appreciation of the MHC formulations and may yield tests of dimensional character and concomitant contribution to electrochemical systems.

First, we reinterpret the classical free energy – reaction coordinate curves depicted in Fig. 1(a) in the context of lower dimensional structures. The initial decrease in ΔG^a followed by a subsequent increase, can be related by analogy to the availability and subsequent lack in the number of energy levels (related to the *DOS*) accessible for electron transfer. Such a modulation is apparent in the *DOS* of one-dimensional nanostructures[28], with increasing carrier concentration and change of the E_F, and may be induced through appropriate η. We have then observed that such non-constant *DOS* yields novel electrical current – voltage response in related electrochemical systems. Fig. 1(b) indicates the correspondence for lower dimensional systems where the decreasing DOS at higher energy may be taken analogous to the increasing λ. Indeed, saturation of the electrical current/rate constant curves may be indicative of the limit of a finite *DOS*.

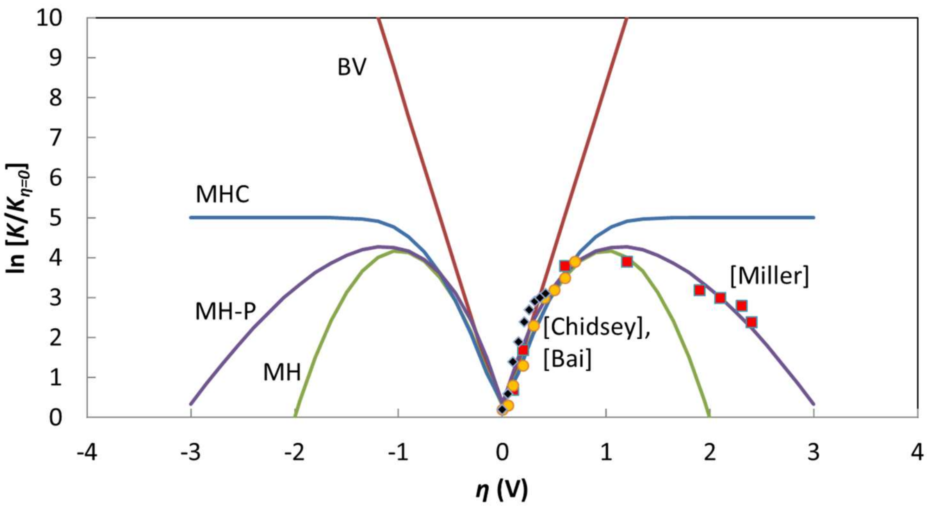

Figure 3-3. The variation of the normalized reaction rate constants, *K,* as a function of electrochemical kinetics, *i.e.,* corresponding to Butler – Volmer: BV, Marcus-Hush: MH, Marcus-Hush-Poisson: MH-P, or Marcus-Hush-Chidsey: MHC, models - with the overpotential η. The *K* values have been normalized to their minimum values in each case. The experimental values were adapted from Miller, *et al.* [26], Chidsey [22], and Bai, *et al,* [29].

The consequent plots of the respective normalized *K* value variation, through Eqns. (1), (2), and (3), with the η (corresponding to BV, MH, or MHC kinetics) are indicated in Fig. 3. From CA related experiments and $I=I_o \exp(-K^{MHC}t)$, such characteristics may be considered equivalent to electrical current I-η plots. The figure also indicates a re-plotting of experimental data previously obtained, and were selected with the rationale that they represented three diverse situations, where nonlinear variation of the rate constant with η was observed, *i.e.,* (1) an inverted region of the rate constant, per M-H kinetics: Miller, *et al*[26], (2) an initial linear variation followed by a saturation of the rate constant, marking the MHC mechanisms: Chidsey[22], and (3) rate constant variation corresponding to electron transfer across solid-solid interfaces typical to carbon coated Li_xFePO_4 crystals: Bai, *et al*[29]. Briefly, the data from Miller, *et al*[26], were obtained through pulse radiolysis experiments on A-Sp-B type (where, A: a molecular group with π–electron network, Sp: a rigid saturated hydrocarbon spacer, and B: 4-biphenylyl) compounds dissolved in either 2-methylytetrahydrofuran (MTHF) or isooctane solvent. The spacer served as a basis to probe inter-molecular electron transfer as a function of its length. The solutions were subject to a 30 ps pulse of solvated electrons and the survival probability of the electrons (measured through the ratio of the absorbance of the solution to that of the solvent alone[30,31]) was estimated. The rate constant was related to the probability, and correlated to the distance over which the electron transfer was effective[30]. A self-assembled alkane thiol monolayer served as a spacer between a ferrocene moiety undergoing a redox reaction and an Au (111) surface, in the experiments by Chidsey[22]. The rate constant, in this case, was monitored through chronoamperometry, through the decay of the electron transfer current in response to an applied potential/voltage step, as previously discussed. In the experiments of Bai, *et al*[29], the rate constants were again extracted through the variation of the transient current with respect to a voltage step, the relative magnitude of which was proportional to the overpotential. The current itself was convoluted from the extent of the phase transformation of $LiFePO_4$ particles. It is to be noted that while the BV kinetics indicates a linear variation (on the semi-log plot) with η, the MH model exhibits a peak as a function of the η. It is also relevant to note that the experimental curves were also fit through employing Poisson statistics [30] assuming homogeneous charge transfer, with a net λ (= 1.2 eV) constituted from (i) an *external* solvation energy $\lambda_s = 0.75$ eV, and (ii) an *internal* vibrational energy component $\lambda_v = 0.45$ eV. The incorporation of Poisson (*cf.,* Gaussian distribution) statistics also yields an inversion of the *K*, while avoiding the steeper drop-off of the MH curve, and was considered [26] the best fit to certain chronoamperometric data.

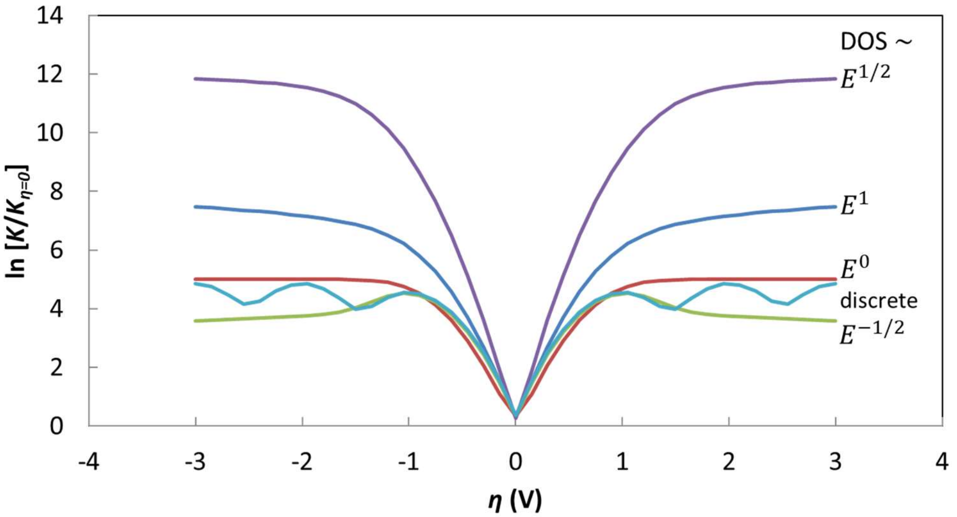

Figure 3-4. The variation of the normalized $K^{MHC\text{-}DOS}$ based reaction rate constants with η - obtained from Eqn. (4), for electrodes with $DOS \sim E^a$. The exponent a, indicated in the figure, is a function of the electrode dimensionality (*i.e., a* = ½ for a three-dimensional semiconductor; *a* = 0 or 1, for a two-dimensional system, *a* = - ½ for a one-dimensional system) and is Delta-function like for zero-dimensional systems, such as quantum dots. The case of *a* = ½ involves a bandgap, which causes the $K_{\eta=0}$ to be smaller than that for the other cases. Generally, a reduction of the *K* corresponds to a decreasing DOS with energy.

We now consider the influence of a variable *DOS* on the *K* variation with η. The number of electrons available for the redox reaction, $n = \int_{E_C}^{\infty} f_{FD}(E - E_F)\ DOS\ (E - E_C)dE$, where E_c is the energy at the bottom of the conduction band. We concomitantly introduce a new *DOS* based reaction rate constant $K^{MHC\text{-}DOS}$, considering the influence of the energy levels, through

$$K^{MHC-DOS} = \ vk_BT\int_{-\infty}^{\infty}\frac{DOS\left(\left|x+\frac{E_F-E_C}{k_BT}\right|\right)}{1+\mathrm{ex}\ \ (x)}exp\left(-\frac{k_BT}{4\lambda}\left[x-\frac{\lambda\mp e\eta}{k_BT}\right]^2\right)dx \quad . (4)$$

The integration may again be either over the negative interval (- ∞, 0] or the positive interval [0, ∞), as previously discussed. In a limiting case corresponding to Eqn. (3), the *DOS* would be a constant (*e.g., ρ*), reverting to the original Chidsey formulation[22]. In the subsequent treatment, the E_c was taken as reference energy and set to zero. Such a formulation involving the energy variation of the DOS[28] as a function of the dimensionality, D (*e.g.,* DOS_{3D} ~ constant or ~ $E^{1/2}$ – for a semiconductor, $DOS_{2D} \sim E^{0}$, $DOS_{1D} \sim E^{-1/2}$, DOS_{0D} ~ Dirac delta function like) also allows for a variable height of the step function, depicted on the left hand side of Fig. 2. The resulting $K^{MHC\text{-}DOS}$-η curves, as a function of the dimensionality dependent *DOS* are indicated in Fig. 4**.** In addition to the parabolic *E-k vector* dispersion, we have also incorporated a linear *E-k* dispersion as seems to be necessary to describe the characteristics of graphene[32] and related 2D materials[33,34].

The respective influences of the dimensionality and the dispersion are clearly evident. While the traditional MHC based formulations assumed a constant *DOS*, particular to bulk-like/three-dimensional (3D) *metallic* electrodes, the energy variation of the *DOS* in lower dimensional systems yields rich and involved behavior. For instance, the behavior of a two-dimensional (2D) material with parabolic energy dispersion, *e.g.,* involving a quantum well, is seen to differ compared to one with linear energy dispersion, *e.g.,* graphene. In the latter case, an increasing *DOS* with electron kinetic energy is responsible for the observed variation. The situation for a one-dimensional (1D) material, *e.g.,* a carbon nanotube (CNT), constituted electrode - with parabolic energy dispersion along the long-axis and quantization along the two perpendicular directions and a decreasing *DOS vis-à-vis* energy - corresponds to inversion in the K-η curves at a sufficiently large η, as posited in the original MH formulations. In one-dimensional systems, the initial increase of the DOS upon the E_F reaching the band edge and the subsequent $E^{-1/2}$ induced decrease yields a corresponding modulation of the K and the electrical currents.

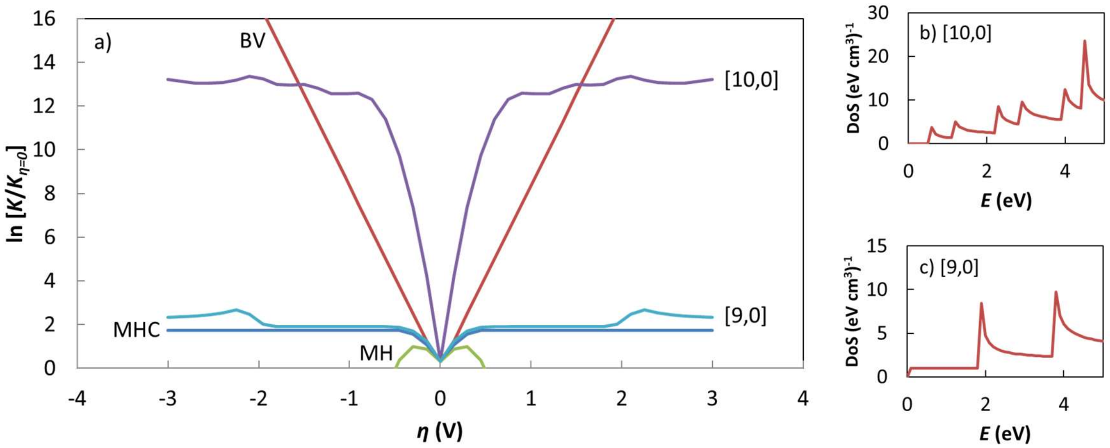

Figure 3-5. **(a)** The predicted variation of the reaction rate constants with η for a [10,0] and [9,0] single-wall CNT with $\lambda = 0.25$ eV. The respective *DOS* (*E*) variation, for the **(b)** [10,0], and **(c)** [9,0] single-wall CNT are indicated. The modulations in the rate constants are due to the successive population and de-population of sub-bands in the nanostructure. E_F was taken to be zero in these simulations.

We then predict the occurrence of oscillations in the $K/K_{\eta=0}$ - η curves in one-dimensional nanostructures as a function of chirality in Fig. 5. As is well known [35], the specific nature of wrapping of a constituent graphene sheet, through the chirality index [*m, n*], dictates whether the resulting CNT is metallic/semiconducting. We depict the corresponding *DOS* for a semiconducting [10,0] nanotube and a metallic [9,0] nanotube: Figures 5(b) and (c), respectively. While *K* oscillations are particularly pronounced in the former, they are less so in the latter case. The underlying reason may be related to the smaller (/larger) separation of the energy sub-bands, respectively. Moreover, the oscillations in the semiconducting and the metallic cases occur at different voltages, corresponding to the *DOS* variation.

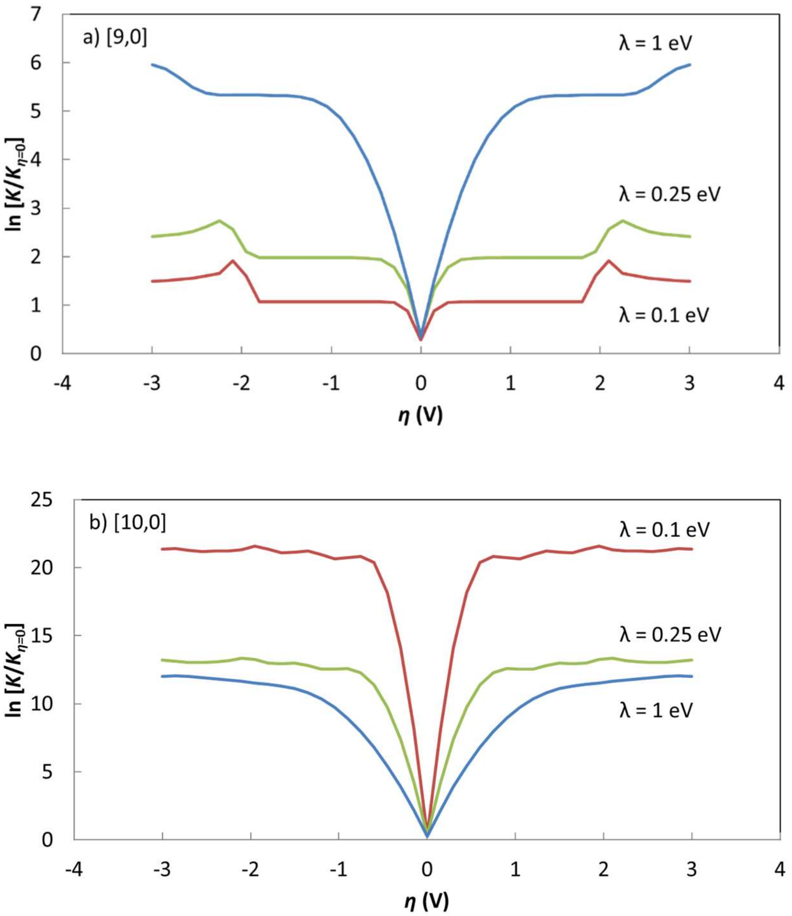

Figure 3-6. The $K/K_{\eta=0}$ variations for a **(a)** [9,0] CNT (carbon nanotube), and **(b)** [10,0] CNT, as a function of the λ, indicates the competing effects of the classical reorganization energy (λ) and the sub-band energy separation (ΔE), with respect to the influence of the *DOS*. The bandgap for the [10,0] CNT actually causes $K/K_{\eta=0}$ to decrease with increasing λ, in contrast to the [9,0] CNT.

We also noted that the width of the energy sub-bands (ΔE) in the electrode considered on the horizontal axis of *DOS* (*E*), with respect to λ - typically electrode adjacent (*e.g.,* electrolyte) side would be another important variable in interpretation of the K-η modulations. Generally, ΔE is indicative of the energy level spacing and inversely related to the size of the nanoscale electrode, *e.g.,* in a one-dimensional CNT of diameter *d*, the equivalent Δ□ would be proportional to $1/d^2$. The magnitude of the λ, as necessary to proceed from an *O* states to an *R* state (as in $O + e^- \rightleftharpoons R$), *cf.,* Fig. 1, can be considered analogous to an energy level width. When ΔE is larger (/smaller) compared to the λ, the interaction of the electrode energy levels (and relevant electron exchange/redox interactions) with respect to the electrolyte would be more (/less) sharply defined and yield an oscillatory (/smooth) K-η variation. A small λ implies that the nuclear reconfiguration and the coordinating solvent interactions [36] accompanying the redox reaction is negligible. At a large enough $\lambda/\Delta E$, a continuous electronic distribution/*DOS* may be assumed yielding smooth MHC kinetics, with an increase of the K up to $\eta \sim \lambda/e$, and subsequent saturation of the K. The discussed K-η variation as related to the $\lambda/\Delta E$ ratio is indicated in Fig. 6. As it was recently indicated that a λ of ~ 0.2 eV seemed to be effective for modeling MHC based charge transfer kinetics at $LiFePO_4$ battery electrode interfaces[29], such modulations could be experimentally probed. Additionally, the $K/K_{\eta=0}$ increases with λ for a [9,0] CNT, as was previously indicated[21], but shows the opposite variation in a [10,0] CNT. The bandgap in the semiconducting [10,0] CNT causes the $K_{\eta=0}$ value to be smaller than that for the metallic [9,0] CNT; such an effect is stronger for smaller λ, *cf.* Fig. 2. We further note that the *net DOS* relevant to the carriers participating in the electrochemical/redox reaction should be considered. Consequently, if the charge carriers from the surface states (*e.g.,* with energy levels inside the bandgap) are involved in the kinetics, then the local *DOS* may need to be considered. The rate constant would be increased at low η due to the surface states and the addition of the LDOS. For high η, because the surface state contribution is generally much smaller than the conduction/valence band contribution, the k trend is not expected to change.

In summary, we have shown that considering the specific nature of the *DOS*, as would be necessary in nanostructured materials, leads to a modification of the expected MHC electro-kinetics. We have predicted, most notably, the occurrence of oscillations of the rate constant and the concomitant electrical current in semiconducting nanotubes, the experimental verification of which would be a significant test of the nature of electrical conductivity as well as dimensionality. The implications of our study would be relevant to the use of nanostructured electrodes in electrochemical storage systems where such electrical current modulations would impact energy and power delivery.

Acknowledgements

The authors are grateful for support from the Defense Advanced Research Projects Agency (DARPA: W911NF-15-2-0122), National Science Foundation (NSF: CMMI 1246800), and acknowledge detailed discussions and interactions with R. Narayanan and Prof. P. M. Asbeck.

Chapter 3, in full, is a reprint of the material as it appears in H. Yamada, P.R. Bandaru, AIP Adv. **6**, 065325 (2016). The dissertation author was the primary investigator and author of this paper.

References

[1] C. Klein and W. Straub, Phys. Rev. **123**, 1581 (1961).

[2] D. Linden and T.B. Reddy, *Linden's Handbook of Batteries* (McGraw Hill, New York, NY, 2010).

[3] S.J. Konopka and B. McDuffie, Anal. Chem. **42**, 1741 (1970).

[4] M. Hoefer and P.R. Bandaru, J. Electrochem. Soc. **160**, H360 (2013).

[5] A.J. Bard and L.R. Faulkner, *Electrochemical Methods: Fundamentals and Applications*, 2nd ed. (John Wiley, New York, 2001).

[6] H.B. Callen, *Thermodynamics* (John Wiley Inc., New York, 1960).

[7] R.S. Muller, T.I. Kamins, and M. Chan, *Device Electronics for Integrated Circuits*, 3rd ed. (John Wiley and Sons, New York, 2003).

[8] N.W. Ashcroft and N.D. Mermin, *Solid State Physics* (Saunders College, Orlando, FL, 1976).

[9] M. Hoefer and P.R. Bandaru, Appl. Phys. Lett. **95**, 183108 (2009).

[10] R.G. Compton and C.E. Banks, *Understanding Voltammetry* (Imperial College Press, London, UK, 2011).

[11] C.M.A. Brett and A.M.O. Brett, *Electrochemistry: Principles, Methods, and Applications* (Oxford University Press, Oxford, 1993).

[12] P.H. Rieger, *Electrochemistry*, 2nd ed. (Chapman and Hall, New York, 1994).

[13] M. Hoefer and P.R. Bandaru, J. Appl. Phys. **108**, 34308 (2010).

[14] Kuznetrsov, *Charge Transfer in Physics, Chemistry and Biology: Physical Mechanisms of Elementary Processes and an Introduction to the Theory* (CRC Press, 1995).

[15] J.-M. Savéant, *Elements of Molecular and Biomolecular Electrochemistry: An Electrochemical Approach to Electron Transfer Chemistry* (John Wiley & Sons, Inc., New York, NY, 2006).

[16] H. Yamada and P.R. Bandaru, Appl. Phys. Lett. **102**, 173113 (2013).

[17] H. Yamada and P.R. Bandaru, Appl. Phys. Lett. **104**, 213901 (2014).

[18] R.A. Marcus, J. Chem. Phys. **24**, 966 (1956).

[19] N. Sutin, J. Phys. Chem. **90**, 3465 (1986).

[20] N.S. Hush, J. Electroanal. Chem. **470**, 170 (1999).

[21] M.C. Henstridge, E. Laborda, N. V. Rees, and R.G. Compton, Electrochim. Acta **84**, 12 (2012).

[22] C.E. Chidsey, Science **251**, 919 (1991).

[23] R.A. Marcus, J. Electroanal. Chem. (2000).

[24] T.M. Cover and J.A. Thomas, *Elements of Information Theory* (Wiley-Interscience, Hoboken, NJ, 2006).

[25] G. Grampp, Angew. Chemie Intl. Edn. **32**, 691 (1993).

[26] J.R. Miller, L.T. Calcaterra, and G.L. Closs, J. Am. Chem. Soc. **106**, 3047 (1984).

[27] T.T.T. Li and M.J. Weaver, J. Am. Chem. Soc. **106**, 6107 (1984).

[28] S. Datta, *Quantum Transport: Atom to Transistor* (Cambridge University Press, New York, 2005).

[29] P. Bai and M.Z. Bazant, Nat. Commun. **5**, 3585 (2014).

[30] J.R. Miller, J. V. Beitz, and R.K. Huddleston, J. Am. Chem. Soc. **106**, 5057 (1984).

[31] J. V. Beitz and J.R. Miller, J. Chem. Phys. **71**, 4579 (1979).

[32] R. Narayanan, H. Yamada, M. Karakaya, R. Podila, A.M. Rao, and P.R. Bandaru, Nano Lett. **15**, 3067 (2015).

[33] M.I. Kastnelson, *Graphene: Carbon in Two Dimensions* (Cambridge University press, Cambridge, UK, 2012).

[34] S. Das Sharma, S. Adam, E.H. Hwang, and E. Rossi, Rev. Mod. Phys. **83**, 407 (2011).

[35] P.R. Bandaru, J. Nanosci. Nanotechnol. **7**, 1239 (2007).

[36] S. Fletcher, J. Solid State Electrochem. **14**, 705 (2010).

[37] P.R. Bandaru, H. Yamada, R. Narayanan, and M. Hoefer, Mater. Sci. Eng. R Reports **96**, 1 (2015).

[38] H. Gerischer, in *CRC Handb. Solid State Electrochem.*, edited by P.J. Gellings and H.J.M. Bouwmeester (CRC Press, Boca Raton, FL, 1997).

[39] A.J. Bard and L.R. Faulkner, *Electrochemical Methods: Fundamentals and Applications*, 2nd ed. (Wiley, Hoboken, 2001).

[40] R. Narayanan, H. Yamada, B.C. Marin, A. Zaretski, and P.R. Bandaru, J. Phys. Chem. Lett. **8**, 4004 (2017).

[41] H. Yamada and P.R. Bandaru, AIP Adv. **6**, 65325 (2016).

[42] R.A. Marcus, Rev. Mod. Phys. **65**, 599 (1993).

[43] N.S. Hush, J. Chem. Phys. **28**, 962 (1958).

[44] H. Yamada and P.R. Bandaru, (2017).

[45] R.S. Muller and T.I. Kamins, *Device Electronics for Integrated Circuits* (Wiley, New York, 1977).

[46] J.R. Schrieffer, Rev. Mod. Phys. **36**, 200 (1964).

[47] J. Bardeen, Phys. Rev. Lett. **6**, 57 (1961).

[48] J. Bardeen, Phys. Rev. Lett. **9**, 147 (1962).

[49] G. Binnig, H. Rohrer, C. Gerber, and E. Weibel, Phys. Rev. Lett. **49**, 57 (1982).

[50] G. Binnig, C.F. Quate, and C. Gerber, Phys. Rev. Lett. **56**, 930 (1986).

[51] W.A. Harrison, Phys. Rev. **123**, 85 (1961).

[52] J.B. Goodenough and Y. Kim, Chem. Mater. **22**, 587 (2010).

[53] W. Zhu, T. Low, V. Perebeinos, A.A. Bol, Y. Zhu, H. Yan, J. Tersoff, and P. Avouris, Nano Lett. **12**, 3431 (2012).

[54] V.M. Pereira, A.H. Castro Neto, H.Y. Liang, and L. Mahadevan, Phys. Rev. Lett. **105**, 156603 (2010).

[55] M. Gilbertini, A. Tomadin, F. Guinea, M.I. Kastnelson, and M. Polini, Phys. Rev. B **85**, 201405(R) (2012).

[56] J. Martin, N. Akerman, G. Ulbricht, T. Lohmann, J.H. Smet, K. von Klitzing, and A. Yacoby,

Nat. Phys. **4**, 144 (2008).

[57] N.L. Ritzert, J. Rodríguez-López, C. Tan, and H.D. Abruña, Langmuir **29**, 1683 (2013).

[58] M.C. Henstridge, C. Batchelor-McAuley, R. Gusmão, and R.G. Compton, Chem. Phys. Lett. **517**, 108 (2011).

4. Electron tunneling in nanoscale electrodes for battery applications

The use of nanostructured materials as electrodes in energy storage devices[37], such as batteries and electrochemical capacitors[17], is typically based on considerations related to a large ratio of the surface area to the volume. An optimal packing of the nanostructures, spanning scales and dimensionality, is necessary to ensure both a large mass-based as well as volume-based energy density, as well as the seamless passage of a large magnitude of concomitant electrical current. Considering the relevance of multi-dimensional current passage, careful attention needs to be paid to the relevant mode of charge transfer both within the electrode, as well as from the electrode to an electrolyte. Generally, electron/carrier transfer occurs when filled states on one side and empty states on the other are aligned[38]. Such an alignment is shifted by an applied voltage difference, *i.e.,* the overpotential, between the electrode and electrolyte. The relationship is reversible, and may be observed experimentally through techniques such as chronoamperometry[22,39,40]. While a theory of electron transfer has been posited based on perturbation theory[36], such formulations typically consider a constant density of states[41] (DOS) in the electrode and a continuum of energy states in the electrolyte[38]. However, in nanostructures, the DOS is highly variable, *e.g.,* as related to the quantum capacitance C_Q[16] in single-layer graphene[32], and non-smooth variations/oscillations of the electrochemical rate constant were predicted in one-dimensional carbon nanotubes, due to chirality dependent DOS[41]. It is the aim of this paper to clarify such foundational aspects, probe alternate viewpoints, and interpret experimental results.

Conventional models, *e.g.* Butler-Volmer (BV)[39], Marcus-Hush (MH)[18,42,43], or Marcus-Hush-Chidsey (MHC)[21,22] kinetics, express traditional electrode battery operation through chemical reaction dynamics, which is chiefly considered through the reaction rate constant k (1/s). These models employ phenomenological constants to relate to the underlying electrochemical processes. This approach is well suited for traditional electrode materials but may not be appropriate for nanomaterials. For instance, in the BV model, α and β are electron transfer coefficients for the chemical reaction (backward and forward, respectively), where $I = I_0$ ($e^{-\alpha\eta}$ + $e^{\beta\eta}$) and $\alpha + \beta = 1$, where η is the overpotential. They represent the ease of reducing the potential barrier for the backward and forward chemical reaction, respectively. In the MH/MHC models, the reorganization energy λ (eV) is taken as a measure of the configurational change related to the species undergoing the redox (*ox*idation or *red*uction) reaction. The Chidsey formalism[22] considers electron occupancy by invoking the Fermi-Dirac distribution, *i.e.,* with $f(E) = 1/(\exp[(E-E_F)/k_BT] + 1)$, with electron energy E, Fermi energy E_F, and thermal energy k_BT. For metallic electrodes, implicitly assuming constant DOS ρ (1/eV) is reasonable. Under this assumption, k saturates when $|\eta| > \lambda/e$, where e is the elementary charge.

However, such an assumption may be unsuitable for nanostructured electrodes. Recent experimental k-η characteristics for single-layer graphene (SLG) electrodes[21,40] do not saturate, and instead monotonically increase with η. A better understanding of such aspects is achieved below by introducing an energy-dependent DOS. The details of this new theory will be presented elsewhere[44].

We first consider the relation between the k and an observed electrical current I (A) to reconcile the experimental data with the energy-dependent DOS theory. k is the net chemical reaction rate for a redox reaction involving oxidized O and reduced R ion species as in $O + e^- \rightleftharpoons R$, and is often experimentally determined[22,39,40] as a time decay constant. For such a reaction,

$$I = FA\left[k_f C_O - k_b C_R\right] \ , \tag{1a}$$

where C_O and C_R (mol/m^2) are the molar concentrations of the O and R species, respectively, and k_f and k_b (1/s) are the forward and backward reaction rate constants, respectively. F (C/mol) is the Faraday constant, and A (m^2) is the electrode-electrolyte contact surface area. For the determination of k_f or k_b alone, large negative or positive η is used, whereby Eqn. (1a) reduces to

$$I = en_{2D}Ak \quad , \tag{1b}$$

where n_{2D} (1/m^2) is the area density of the relevant ion species and $k = k_f$ or k_b. The nanostructured experimental data may thus be written equivalently in terms of k or I.

When considering charge transfer through electron transport, I is defined as

$$I = eAnv \quad , \tag{2a}$$

where n (1/m^3) is the electron carrier density and v (m/s) is the electron velocity. The shift from k to v allows us to discuss spatial coordinates. However, such a specific form is relevant for current flow through a homogeneous material. I from the electrode to the electrolyte (or vice versa) may be broadly described through an equation of the form

$$I = eAnv\Theta \quad , \tag{2b}$$

with Θ as the tunneling probability of the electrons participating in the redox reaction[45,46].

Considering Eqn. (2b) in more depth, it is necessary to use both $f(E)$ and the DOS for both the electrode and the electrolyte to determine A, n, and v, as well as the coefficient from Fermi's Golden Rule to determine v and Θ[47–50]. Consequently,

$$I_{lt} = e\int[f_{eld} \times A\ell D_{3D}]\frac{2\pi}{\hbar}M^2[(1-f_{rdx}) \times \rho]dE \ , \tag{3a}$$

$$I_{rt} = e\int[(1-f_{eld}) \times A\ell D_{3D}]\frac{2\pi}{\hbar}M^2[f_{rdx} \times \rho]dE \ . \tag{3b}$$

Here, I_{lt} represents left-going current (right-going electrons) and I_{rt} represents right-going current (left-going electrons). The equation explicitly considers the electrode DOS $D(E)$ (1/(eV m^3)) and occupancy probability f_{eld} (E) with Fermi energy E_F, and the electrolyte DOS (integrated over volume) $\rho(E)$ (1/eV) and occupancy probability $f_{rdx}(E)$ with redox energy E_{rdx}. Depending on the dimensionality of D, a spatial normalization representing the active electrode region is multiplied, e.g. a volume $A\ell$ (3D), an area A (2D), a length ℓ (1D), or nothing (0D), such that the normalization times D has units of 1/eV. $\hbar$ (eV s) is the Planck constant, and the matrix element of interaction M (eV) couples the electrode and electrolyte energy levels, smaller in magnitude compared to the level broadening, and hence considered to be relatively energy independent[51]. The electrolyte properties and matrix element together represent the Fermi's Golden Rule, which describes electron transfer rate. Moreover, for the occupancy probability distribution, the Fermi-Dirac distribution was considered over the Boltzmann distribution for both electrode and electrolyte to represent the occupancy of the states, and implicitly considers electron – electrolyte interactions. Typically, ρ may be considered through a Gaussian: $\rho(\Delta E) = \rho_0 \exp\left[-(\Delta E)^2/(4\lambda k_B T)\right]$. The ΔE is related to the deviation of a redox species electron energy from the most probable energy, corresponding to say, that for reduction (*red*) or oxidation (*ox*), *i.e.,* $\Delta E = \Delta E_{red}$ $(= E_{red} - E_{red}^{o})$ or

$\Delta E = \Delta E_{ox}$ ($= E_{ox} - E_{ox}^{o}$). The electrolyte DOS is represented through two peaks for the *red* and *ox* levels, which may be correlated to electron affinity and ionization energy, with a range of energies and corresponding states. Moreover, the possibility of a solid electrolyte may be easily understood through considering the ρ of a solid as well as replacing E_{rdx} with another E_F, distinct from the electrode's E_F. It is then interesting to note that the electrolyte dimensionality may need to be considered in the performance of a related device, *e.g.,* a solid-state battery. For instance, a confined two-dimensional electrolyte may yield significantly enhanced power due to a step-like onset of the electrical current with increased voltage[28].

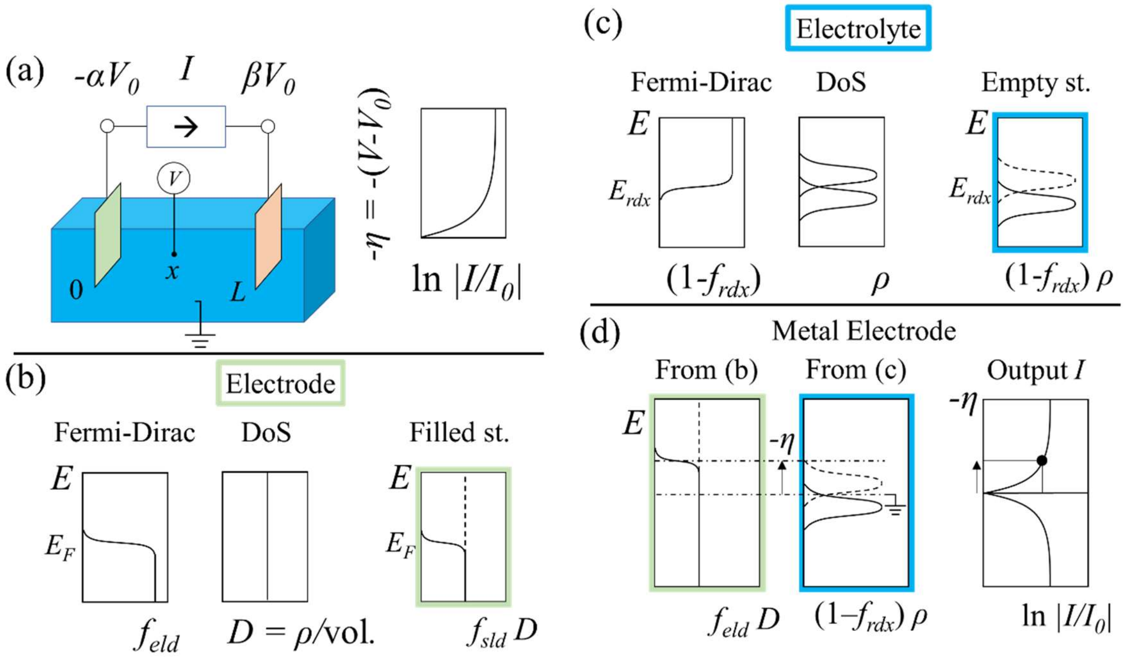

Figure 4-1. **(a)** The consideration of electrode dimensionality of nanoscale electrodes, together with electrode-electrolyte interactions in a typical electrochemical system (*e.g.,* a battery or capacitor), yields novel electrokinetics. α and β are electron transfer coefficients for the voltage, most often used in the Butler-Volmer model; $\alpha + \beta = 1$. The consequent electrical current I with respect to an overpotential η (with the standard redox potential as a reference) and normalized to I_o, the current at $\eta = 0$, is due to the mutual overlap of the carrier density from the electrode with the electrolyte. **(b)** The product (*right*) of the electrode Fermi-Dirac function $f_{eld}(E)$ (*left*) and DOS $D(E)$ (*middle*). D can be converted to units of eV^{-1} by multiplying electrode volume for a 3D material. **(c)** The product (*right*) of the reverse of the electrolyte Fermi-Dirac function $1\text{-}f_{rdx}(E)$ (*left*) and DOS $\rho(E)$ (*middle*). **(d)** ln $|I/I_0|$, represented by the convolution (*right*) of $f_{eld}\, D$ (*left*) and $(1\text{-}f_{rdx})\, \rho$ (*middle*).

It is to be noted that the use of a constant DOS for D is acceptable, so long as the applied voltage range is less than $|E_F - E_C|$: Figure 1. Here, the product of the respective f with the distribution of the O and the R species in the electrolyte – per Eqn. (3) yields an electrical current variation with η of the MHC type: Figure 1d, with a saturation at $\eta > \lambda$. The electrical currents have been normalized to the equilibrium current value I_o (the current at $\eta = 0$). If a constant DOS is assumed, the result is a curve consistent with the MHC theory. Furthermore, if λ is taken to an infinite limit, the result is a line consistent with the BV theory.

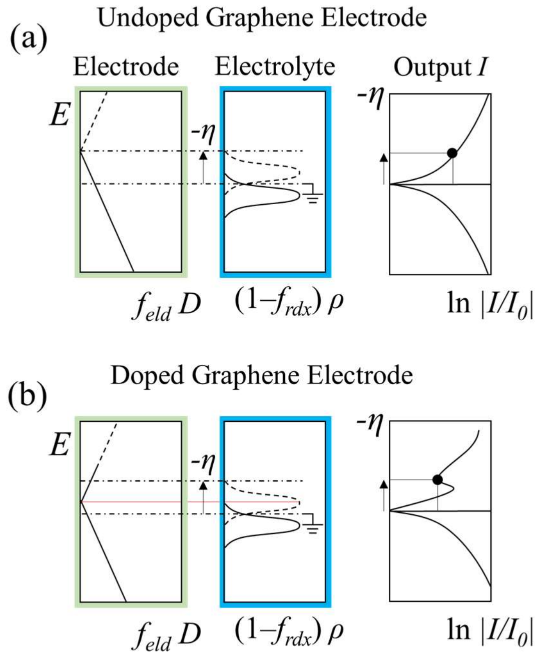

Figure 4-2. A non-monotonic $I(\eta)/I_0$ variation for **(a)** defect-free/pristine, and **(b)** defective/n-doped graphene. The variation closely follows the relevant DOS shape. A dip is observed in the latter case, when the Dirac point eventually aligns with the electrolyte DOS peak.

We investigate the implications of Eqn. (3) for other low-dimensional electrodes, where there would be considerable variation in the corresponding DOS. For example, in the case of single layer graphene (SLG) with $D \sim E$, and in contact with an electrolyte, we obtain a $I(\eta)/I_0$ variation indicated in Figure 2a for the defect-free/pristine case ($E_F = 0$). The remarkable aspect here is that I does not saturate as in MHC kinetics but instead monotonically increases with η over a considerable range mimicking the DOS variation, and would be dictated only by the electrolyte stability limits[52]. Higher η values result in more graphene electrode states being continually aligned with the electrolyte. It is again assumed that f can be approximated by a step function - applicable when η exceeds 26 mV ($=k_BT/e$). However, the inevitable presence of defects (*e.g.,* structural wrinkles[53,54], electron-hole puddles[32,55,56], *etc.*) on graphene has been well documented and for such an unintentionally doped material, $E_F > 0$ assuming *n*-type doping. In this case: Figure 2b, there would be an initial monotonic variation with η followed by a dip in the $I(\eta)/I_0$ vs. η plot, when the Dirac point eventually aligns with the electrolyte DOS peak, beyond which there would be an increase again.

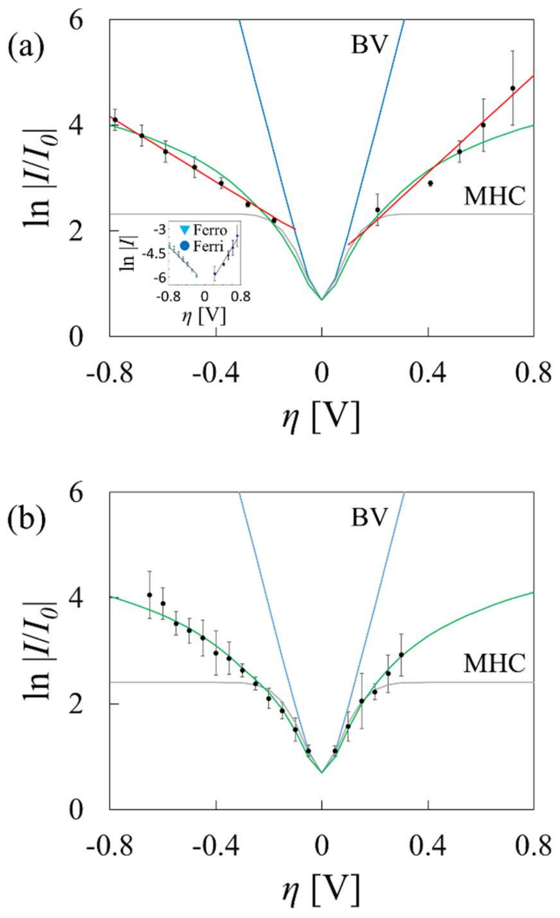

Figure 4-3. Modeling the experimentally obtained reaction rate/electric current variation for **(a)** single layer graphene, using the formalism relevant to Eqn. (3), yields a more physical fit than BV kinetics as used by Ritzert, *et al* [57] *– see inset*. $\alpha = 0.08$ and $\beta = 0.12$, which is in conflict with the free energy conservation restriction of $\alpha + \beta = 1$. **(b)** Another independent confirmation of the necessity of DOS considerations from our own experiments[40] with a finite DOS at the Dirac point.

While such interesting features in I need experimental confirmation, we have seen both in our own experiments and those in literature the need for explicitly considering the dimensionality relevant DOS. For instance, the oxidation and reduction kinetics of ferricyanide at SLG electrodes was fit to BV kinetics[57] – see inset to Figure 3a. However, a more detailed analysis indicates unequal forward and backward electron transfer coefficients of 0.08 and 0.12 respectively, with a sum less than unity. However, a sum of unity is required[36] from fundamental thermodynamic considerations related to microscopic reversibility[58]. Alternately, the use of Eqn. (3) for the electrical current yields a much better fit: Figure 3a, compared to BV kinetics. Yet another independent confirmation of the necessity of DOS considerations is indicated by our own experiments[40] on defective SLG with a finite DOS at the Dirac point, with the data and fit plotted in Figure 3b.

(a) Nanowire Electrode

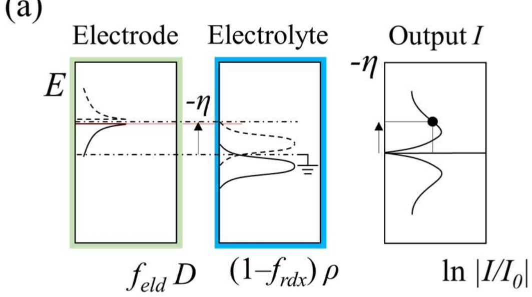

(b) Quantum Dot Electrode

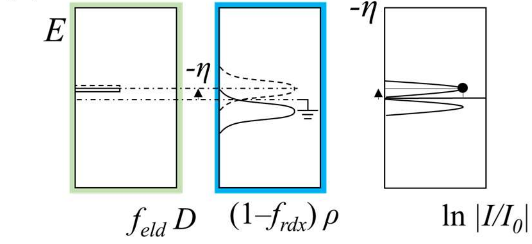

Figure 4-4. A decrease in the electrical current $I(\eta)$, with increasing η is predicted in **(a)** one-dimensional structures, such as single-walled carbon nanotubes, and **(b)** in zero-dimensional quantum dots, due to a depletion of constituent electrical carriers.

The implications of considering the specific DOS of the electrode as well as the electrolyte were also extended to one-dimensional (*e.g.,* carbon nanotubes) or zero-dimensional (*e.g.,* quantum dot) based systems. From the aspect that I is an indicator of the integrated DOS variation, we see that for one-dimensional structures where $D \sim E^{-1/2}$, that there is actually a reduction in the current with increasing η: Figure 4a, while a delta-function like DOS in quantum dots, with a finite number of states yields a concomitant limited range of η over which a finite current may be obtained: Figure 4b.

In summary, electron tunneling, considering energy-dependent DOS of the electrode and the electrolyte, may be used to describe current flow in electrochemical systems deploying nanostructured electrodes. We have indicated the possibilities of unique signatures of electrical current variation that may be obtained in electrochemical systems through specific consideration of the DOS variations of nanoscale electrodes. The related formulations are interesting as they predict a non-monotonic variation, in distinct contrast to conventional BV and MHC kinetics, of the electrical current with increasing voltage. The derived equations are adaptable to systems with solid electrolytes and would enable estimates of the maximal current and expected efficiency.

Acknowledgments

The authors are grateful for support from the Defense Advanced Research Projects Agency (DARPA: W911NF-15-2-0122) and the National Science Foundation (NSF: CMMI 1246800 and CBET 1606192). Fruitful discussions with Prof. Peter M. Asbeck are greatly appreciated.

Chapter 4, in full, is a reprint of the material as it appears in H. Yamada, R. Narayanan, P. R. Bandaru, Chem. Phys. Lett. **695**, 24-27 (2018). The dissertation author was the primary investigator and author of this paper.

References

[1] C. Klein and W. Straub, Phys. Rev. **123**, 1581 (1961).

[2] D. Linden and T.B. Reddy, *Linden's Handbook of Batteries* (McGraw Hill, New York, NY, 2010).

[3] S.J. Konopka and B. McDuffie, Anal. Chem. **42**, 1741 (1970).

[4] M. Hoefer and P.R. Bandaru, J. Electrochem. Soc. **160**, H360 (2013).

[5] A.J. Bard and L.R. Faulkner, *Electrochemical Methods: Fundamentals and Applications*, 2nd ed. (John Wiley, New York, 2001).

[6] H.B. Callen, *Thermodynamics* (John Wiley Inc., New York, 1960).

[7] R.S. Muller, T.I. Kamins, and M. Chan, *Device Electronics for Integrated Circuits*, 3rd ed. (John Wiley and Sons, New York, 2003).

[8] N.W. Ashcroft and N.D. Mermin, *Solid State Physics* (Saunders College, Orlando, FL, 1976).

[9] M. Hoefer and P.R. Bandaru, Appl. Phys. Lett. **95**, 183108 (2009).

[10] R.G. Compton and C.E. Banks, *Understanding Voltammetry* (Imperial College Press, London, UK, 2011).

[11] C.M.A. Brett and A.M.O. Brett, *Electrochemistry: Principles, Methods, and Applications* (Oxford University Press, Oxford, 1993).

[12] P.H. Rieger, *Electrochemistry*, 2nd ed. (Chapman and Hall, New York, 1994).

[13] M. Hoefer and P.R. Bandaru, J. Appl. Phys. **108**, 34308 (2010).

[14] Kuznetrsov, *Charge Transfer in Physics, Chemistry and Biology: Physical Mechanisms of Elementary Processes and an Introduction to the Theory* (CRC Press, 1995).

[15] J.-M. Savéant, *Elements of Molecular and Biomolecular Electrochemistry: An Electrochemical Approach to Electron Transfer Chemistry* (John Wiley & Sons, Inc., New York, NY, 2006).

[16] H. Yamada and P.R. Bandaru, Appl. Phys. Lett. **102**, 173113 (2013).

[17] H. Yamada and P.R. Bandaru, Appl. Phys. Lett. **104**, 213901 (2014).

[18] R.A. Marcus, J. Chem. Phys. **24**, 966 (1956).

[19] N. Sutin, J. Phys. Chem. **90**, 3465 (1986).

[20] N.S. Hush, J. Electroanal. Chem. **470**, 170 (1999).

[21] M.C. Henstridge, E. Laborda, N. V. Rees, and R.G. Compton, Electrochim. Acta **84**, 12 (2012).

[22] C.E. Chidsey, Science **251**, 919 (1991).

[23] R.A. Marcus, J. Electroanal. Chem. (2000).

[24] T.M. Cover and J.A. Thomas, *Elements of Information Theory* (Wiley-Interscience, Hoboken, NJ, 2006).

[25] G. Grampp, Angew. Chemie Intl. Edn. **32**, 691 (1993).

[26] J.R. Miller, L.T. Calcaterra, and G.L. Closs, J. Am. Chem. Soc. **106**, 3047 (1984).

[27] T.T.T. Li and M.J. Weaver, J. Am. Chem. Soc. **106**, 6107 (1984).

[28] S. Datta, *Quantum Transport: Atom to Transistor* (Cambridge University Press, New York, 2005).

[29] P. Bai and M.Z. Bazant, Nat. Commun. **5**, 3585 (2014).

[30] J.R. Miller, J. V. Beitz, and R.K. Huddleston, J. Am. Chem. Soc. **106**, 5057 (1984).

[31] J. V. Beitz and J.R. Miller, J. Chem. Phys. **71**, 4579 (1979).

[32] R. Narayanan, H. Yamada, M. Karakaya, R. Podila, A.M. Rao, and P.R. Bandaru, Nano Lett. **15**, 3067 (2015).

[33] M.I. Kastnelson, *Graphene: Carbon in Two Dimensions* (Cambridge University press, Cambridge, UK, 2012).

[34] S. Das Sharma, S. Adam, E.H. Hwang, and E. Rossi, Rev. Mod. Phys. **83**, 407 (2011).

[35] P.R. Bandaru, J. Nanosci. Nanotechnol. **7**, 1239 (2007).

[36] S. Fletcher, J. Solid State Electrochem. **14**, 705 (2010).

[37] P.R. Bandaru, H. Yamada, R. Narayanan, and M. Hoefer, Mater. Sci. Eng. R Reports **96**, 1 (2015).

[38] H. Gerischer, in *CRC Handb. Solid State Electrochem.*, edited by P.J. Gellings and H.J.M. Bouwmeester (CRC Press, Boca Raton, FL, 1997).

[39] A.J. Bard and L.R. Faulkner, *Electrochemical Methods: Fundamentals and Applications*, 2nd ed. (Wiley, Hoboken, 2001).

[40] R. Narayanan, H. Yamada, B.C. Marin, A. Zaretski, and P.R. Bandaru, J. Phys. Chem. Lett. **8**, 4004 (2017).

[41] H. Yamada and P.R. Bandaru, AIP Adv. **6**, 65325 (2016).

[42] R.A. Marcus, Rev. Mod. Phys. **65**, 599 (1993).

[43] N.S. Hush, J. Chem. Phys. **28**, 962 (1958).

[44] H. Yamada and P.R. Bandaru, (2017).

[45] R.S. Muller and T.I. Kamins, *Device Electronics for Integrated Circuits* (Wiley, New York, 1977).

[46] J.R. Schrieffer, Rev. Mod. Phys. **36**, 200 (1964).

[47] J. Bardeen, Phys. Rev. Lett. **6**, 57 (1961).

[48] J. Bardeen, Phys. Rev. Lett. **9**, 147 (1962).

[49] G. Binnig, H. Rohrer, C. Gerber, and E. Weibel, Phys. Rev. Lett. **49**, 57 (1982).

[50] G. Binnig, C.F. Quate, and C. Gerber, Phys. Rev. Lett. **56**, 930 (1986).

[51] W.A. Harrison, Phys. Rev. **123**, 85 (1961).

[52] J.B. Goodenough and Y. Kim, Chem. Mater. **22**, 587 (2010).

[53] W. Zhu, T. Low, V. Perebeinos, A.A. Bol, Y. Zhu, H. Yan, J. Tersoff, and P. Avouris, Nano Lett. **12**, 3431 (2012).

[54] V.M. Pereira, A.H. Castro Neto, H.Y. Liang, and L. Mahadevan, Phys. Rev. Lett. **105**, 156603 (2010).

[55] M. Gilbertini, A. Tomadin, F. Guinea, M.I. Kastnelson, and M. Polini, Phys. Rev. B **85**, 201405(R) (2012).

[56] J. Martin, N. Akerman, G. Ulbricht, T. Lohmann, J.H. Smet, K. von Klitzing, and A. Yacoby,

Nat. Phys. **4**, 144 (2008).

[57] N.L. Ritzert, J. Rodríguez-López, C. Tan, and H.D. Abruña, Langmuir **29**, 1683 (2013).

[58] M.C. Henstridge, C. Batchelor-McAuley, R. Gusmão, and R.G. Compton, Chem. Phys. Lett. **517**, 108 (2011).

5. Modulation of the electrostatic and quantum capacitances of few layered graphenes through plasma processing

A comprehensive understanding of the characteristics of graphene[1] with regard to its unique electrical and structural attributes would be incomplete unless the inevitable presence of defects have been considered. While such imperfections may limit[2] the realization of theoretically redicted characteristics, they may also be vital for uncovering new fundamental phenomena and related applications. Here we show that the charged defect generation, through argon ion based plasma processing, in few layer graphene (FLG) could be integral to the substantial enhancement of the electrical capacitance and be of potential use[3] in electrochemical (EC) energy storage.[4] By combining EC characterization techniques with detailed Raman spectroscopic analysis, we elucidate the contributions of plasma-induced defects to electrostatic and quantum capacitance.

The FLG-based structures were synthesized on Ni foil substrates through chemical vapor deposition and the detailed synthesis procedures have been outlined previously (in the Methods section of ref 5). The prepared FLGs (referred to hereafter, as “pristine”) were subsequently subjected to argon based plasma processing to intentionally[6] induce charged defects. Argon was chosen because the constituent ionic species are limited[7] to Ar^+, implying relatively simple plasma chemistry.[8] The plasma processing was carried out in a customized reactive ion etching chamber with an electrode bias (~ -100 V) and an ion density[9] of the order of 10^{11} /cm^3. The applied electrical power (in watts), which would be proportional to the electric field between the electrodes in the chamber, was used as a parameter to tune the extent of Ar^+ graphene interaction over a range of time. It was hypothesized, based on previous experimental evidence,[10] that dangling bond rich[11] edge plane defects could be created in the FLGs during Ar plasma exposure through the removal of carbon atoms,[10] see Figure 1a.

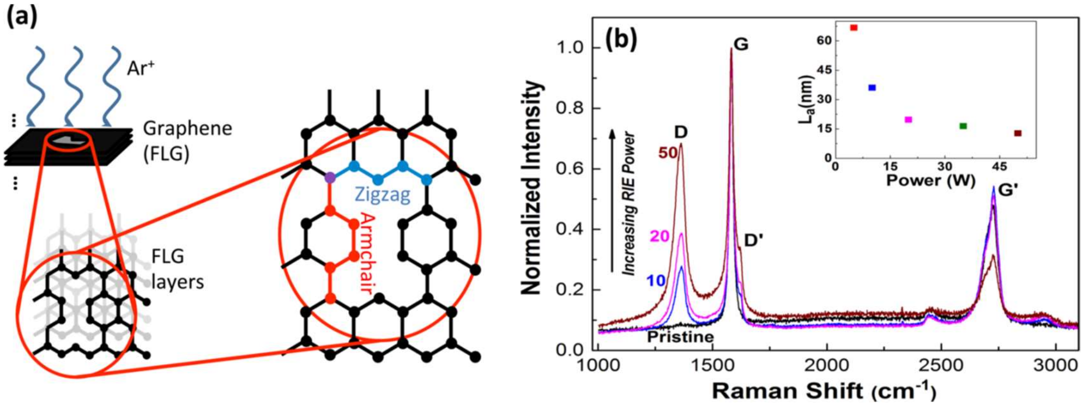

Figure 5-1. Artificial introduction of charged states in few layer graphenes. (a) Argon ion based plasma processing was used to purposefully create defects, such as dangling bond rich edge plane defects of the armchair or zigzag varieties, in few layer graphene (FLG) structures. (b) Enhanced plasma processing applied to the pristine sample, results in a substantial intensity enhancement of the D- and D′-peaks as seen in the Raman spectra (normalized to the G-peak). An increase in power, say to 50 W, may result in irreversible changes due to graphene removal. The plot of the Tuinstra−Koenig correlation length (La) obtained from the area integrated D- to G-peak intensity ratio is shown in the inset and indicates decreased crystallite size with increased plasma power.

Considering that the formation energy of extended defects (∼1.1 eV for divacancy)[2] is significantly smaller than point defects (∼7 eV), the creation of pores (or extended defects) in graphene with chiral edges (i.e., containing a combination of armchair: AC, and zigzag: ZZ, type edges) is expected. Subsequently, the structural attributes of the processed FLG films were analyzed through Raman spectroscopy to characterize the effects of plasma processing; see Figure 1b. The relative variation of the D-peak observed at ∼1350 cm^{-1} (which is disorder induced and originates from higher order electron−phonon scattering processes) with respect to the G-peak at ∼1580 cm^{-1} (which arises due to normal first order scattering processes in graphene) was used as an initial metric.[12] The normalization of the Raman peaks was done with respect to the G-peak, per convention. It was seen that while the pristine FLG has an A_D/A_G ratio close to zero (where A refers to the net area integrated intensity of the respective peak), there was a substantial increase of the D-peak intensity with increasing Ar^+ plasma exposure.[13] The A_D/A_G ratio has often been used, through the Tuinstra-Koenig relation[14,15] (typically adapted[16] through $A_D/A_G = (560/E_L^4)(1/L_a)$, where E_L is the input laser energy, in electron volts) as a measure of an effective crystallite size/correlation length (L_a) in nanographites; see inset Figure 1b. Concomitantly, the G' peak feature at ~2700 cm^{-1} (close to the second harmonic of the D-peak and characteristic of double/triple resonance processes in graphenes[12]) was also observed. It is well-known that the deconvolution of the G'-peak into either a single peak or multiple peaks is indicative of the state of the graphene, that is, the number as well as orientation of the layers in the FLGs.[17] The decrease of the G'-peak intensity seen in Figure 1b concurs with the enhancement in D-peak intensity, due to the defects induced by high plasma processing power.

While the D-peak increase in the processed FLGs seems to record a net increase in defect content, it has also been indicated that this feature is typical to AC edges and not of ZZ edge type defects based on momentum conservation principles.[18] An important attribute of ZZ defects is that they may be electrically active and could contribute to an enhanced density of states (DOS) near the Fermi energy (E_F),[19] much more than the AC type edge defects (which contribute less due to the two constituent carbon atoms belonging to different sublattices[16]).

In this context, a nanostructure characteristic that is DOS specific is the quantum capacitance,[20,21] C_Q, which is defined through (see Section I.a of Supporting Information)

$$C_Q = e^2 DOS(E_F) = e^2 \sqrt{\frac{4}{\pi}\frac{n_{2D}}{(\hbar v_F)^2}} \quad . \tag{1}$$

In the above relation, e is the unit of elementary electronic charge, n_{2D} is the carrier density (in cm^{-2}) of the 2D graphene, $\hbar$ is the reduced Planck constant (= 1.05×10^{-34} Js), and v_F is the Fermi velocity in m/s. We have previously shown[22] through electrochemical characterization that the C_Q

is in series with the nominal double-layer capacitance, C_{dl}, and could be inferred through the total measured capacitance C_{meas}. However, for the six-layer FLG used in our studies (see Figure S2 in the Supporting Information), it may also be necessary to incorporate a space charge capacitance[23] C_{SC}, which arises due to the screening of the electrolyte charge in the inner graphene layers by the outer graphene layers, and which would also be in series with C_{dl} (also see Section I.e of the Supporting Information). We consider the relevant length scale for the charge storage to be defined over an equivalent Thomas–Fermi screening length[24] λ_{TF} with C_{SC} given by

$$C_{sc} = \frac{\epsilon}{\lambda_{TF}} = \sqrt{\frac{2\epsilon e^2 n}{E_F}} \ . \tag{2}$$

ε is the dielectric permittivity (~$5.7\varepsilon_0$ for graphene[6], where $\varepsilon_0 = 8.854 \times 10^{-12}$ F/m) and n is the carrier density per unit volume in units of cm^{-3}. Consequently, the individual contributions to the C_{meas} would be manifested through

$$\frac{1}{C_{meas}} = \frac{1}{C_{dl}} + \frac{1}{C_Q} + \frac{1}{C_{SC}} \ . \tag{3}$$

For insight into C_Q and C_{SC} of plasma processed FLGs, we conducted cyclic voltammetry (CV) of FLG-based electrodes (as the working electrode in a three electrode setup) in an organic electrolyte consisting of 0.25 M tetrabutylammonium hexafluorophosphate (TBAHFP) dissolved in 1 M acetonitrile. The area enclosed by the CV curves divided by the voltage scan rate (ν) is directly related to the net charge and was used to estimate the C_{meas}. The absence of peaks in the CV plots indicates the lack of redox reactions and faradaic capacitance (CF) contributions[26]. It was seen that C_{meas} increased substantially as a function of the Ar+ plasma power. The more than doubling of the C_{meas} from 1.9 μF/cm^2 (for the pristine sample) to 4.7 μF/cm^2 (for the sample subject to 20 W plasma) is remarkable and suggests a novel means of substantially enhancing capacitance.

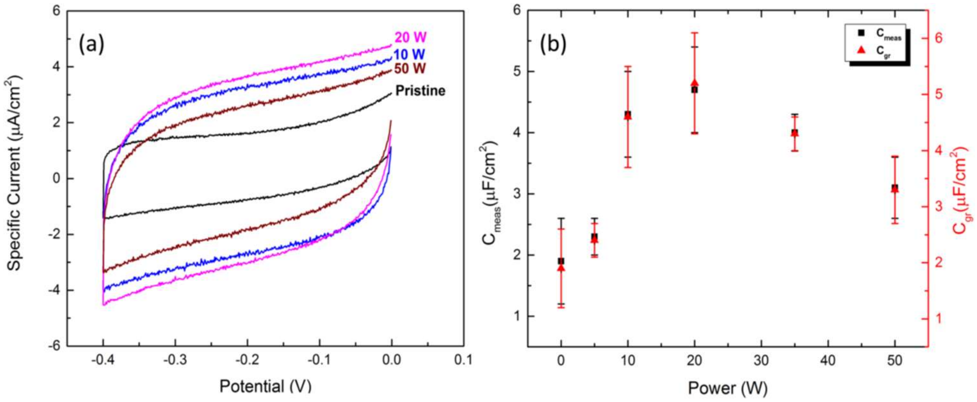

Figure 5-2. Electrochemical characterization of argon plasma processed FLGs. (a) CV characterization of plasma processed FLG samples (in 0.25 M TBAHFP dissolved in a 1 M acetonitrile). The area enclosed by the CV curves was used to parametrize the C_{meas}, which increases with plasma power (indicated on the figure). (b) A close to 3-fold enhancement in the C_{meas} (left axis) and the aggregated contributions of the computed C_{SC} and the C_Q (right axis), i.e., $1/C_{gr} = 1/C_{SC} + 1/C_Q$, as a function of the plasma power. The C_{gr} is in series with the nominal double-layer capacitance and is related to the induced charged defect density.

While it is indicated in Figure 2b that increased power (for example, at and beyond 35 W) causes a reduction in the C_{meas}, the decrease may be due to the strong lattice disruption and/or etching away of graphene as suggested through Raman spectra and optical microscopy. It was ensured that the Ni substrate was not involved in such estimates. We do not use the F/g metric for reporting the capacitance values as is often done in extant literature, as the specific surface area (in m^2/g) is (a) not well-known, and (b) not easily measurable. Indeed, there have been a lot of exaggerations in literature through the use of the theoretical SSA.

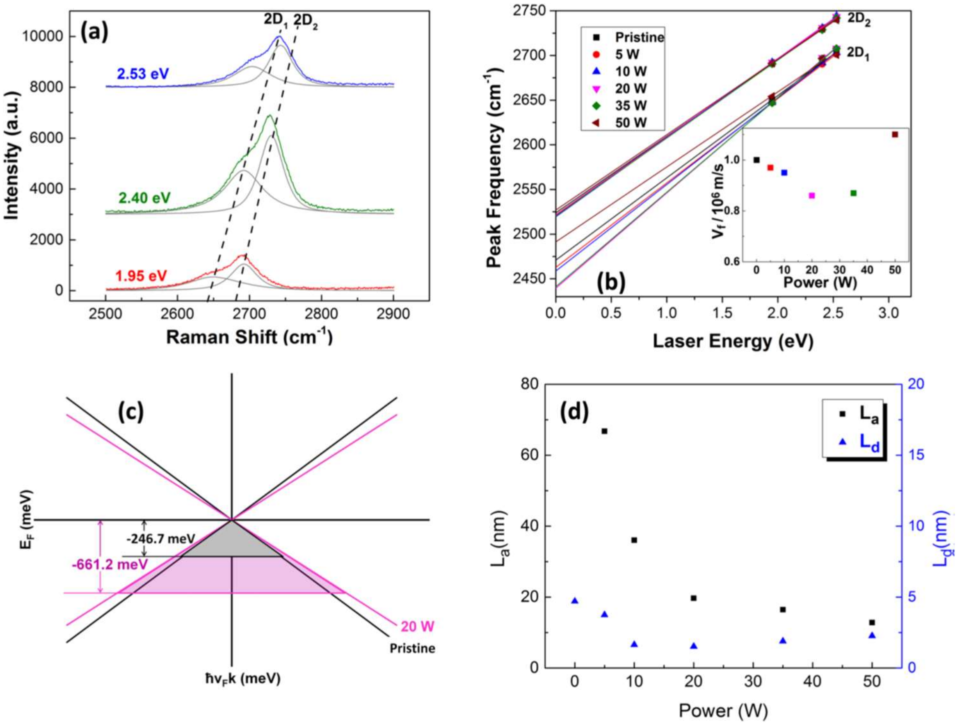

Figure 5-3. Determination of the charge configurations and charge correlation length scales. (a) The energy dispersion of the G'-peak indicated a blue shift and was composed of individual variation of the deconvolved $2D_1$ and $2D_2$ constituents. The laser energies, used for the Raman spectroscopy, are indicated on the individual plots. The relatively prominent left shoulder as well as the overall peak width (of ~70 cm^{-1}) seems to indicate a HOPG character to the processed FLGs. (b) The variation of the $2D_1$ and $2D_2$ peak frequency ($\omega_{G'}$) with Raman laser energy was fit to a straight line, as expressed through $\omega_{G'} = aE_L + b$ with a related to the phonon velocity/Fermi velocity (v_F) ratio and b indicative of the phonon frequency at the K-point of the Brillouin zone. A larger change in the a was seen for the $2D_1$ peak and was used to infer a v_F modulation due to plasma processing. The inset shows the variation of the computed v_F with plasma power. (c) While the interlayer interaction in FLG has been implicated in a nonlinear energy dispersion, for example, a hyperbolic dispersion for bilayer graphene in the vicinity of the E_F, a linear E−k energy dispersion relation could be considered[34] for insight. The plasma processing introduced positive charges akin to p-type doping into the FLG. The enhanced charge density increased the EF from ~247 to ~661 meV (at 20 W plasma power), which was reckoned with respect to E = 0 point, along with a reduced v_F that was indicated by the decreased slope. (d) A charge correlation length, L_d (right axis), as deduced from the carrier density in the graphene sheet closest to the electrolyte, was smaller compared to the Tuinstra−Koenig correlation length, L_a (left axis), as deduced from Raman spectroscopy.

Using nominally identical electrolyte and experimental conditions and assuming that the C_{dl} would be a function only of the electrolyte concentration[26], an increased current in the voltammogram while the shape remains nearly rectangular is characteristic of additional capacitance contributions from C_{SC} and C_Q. For calibration of the constituents of C_{meas}, we used the bare Ni foil substrate, the C_{SC} and C_Q values of which would be effectively very large due to its metallic nature. C_{meas} would then be close to C_{dl} from Eqn. (3). A value for C_{dl} of around 20 μF/cm^2 was measured for polished Ni foil. It should be noted that any enhancement possibly due to the area increase brought about by, for example, a change in surface topography[27] would only further minimize the C_{dl} contribution and not substantially alter the conclusions. The discrepancy between C_{meas} (in FLG samples), as in Figure 2b, and C_{dl} (obtained from Ni foil experiments) could then be attributed to C_{SC} and C_Q of the FLG. We then proceeded to evaluate the relative partitioning of C_{SC} and C_Q from Eqns. (1) and (2). In addition to the knowledge of v_F, n_{2D} (for understanding the variation of C_Q) and n (for C_{SC}) and the related E_F must be recognized and estimated.

The vF was noted using Raman spectroscopy through considering the dispersion of the G'-peak frequency (ω G') with laser energy (E_L). Such a variation has previously been understood[28] in terms of a relation of the form: ω G' = $aE_L + b$, where a is the ratio[29] of the respective phonon velocity, v_{ph}, to the v_F near the K-point of the Brillouin zone. The b connotes the in-plane transverse optical phonon (iTO) frequency at the K-point with a larger value marking a hardening of the phonon mode frequency. The G'-peak, from Figure 1b could be adequately fitted through deconvolution into two peaks: Figure 3a, termed $2D_1$ (smaller energy/wavenumber peak) and $2D_2$ (the higher wavenumber peak). The relatively prominent left shoulder to the peak as well as the overall peak width (of ~70 cm^{-1}) may be indicative of highly oriented pyrolytic graphite (HOPG)-like character.[30] By plotting the energy dispersions of the $2D_1$ and $2D_2$ peaks at three laser energies (1.96 eV, 633 nm; 2.41 eV, 514 nm; and 2.54 eV, 488 nm), as shown in Figure 3b, we obtained increasing a values for the $2D_1$ peak as a function of plasma processing power (enhanced by ~16%; from ~92 cm^{-1}/eV for the pristine sample to ~107 cm^{-1}/eV for the 20 W processed sample) with a much smaller change for the $2D_2$ peak, from ~86 cm^{-1}/eV in the pristine sample to ~88 cm^{-1}/eV for the 20 W sample. Concomitantly, the b values for the $2D_1$ peak varied by ~1% on the application of plasma power, with a much smaller change for the $2D_2$ peak; see intercepts in Figure 3b. Because of the small change of the b, we assumed a relative constancy of the v_{ph} and the origins of the change in a, for example, for the $2D_1$ peak, to be mostly from a change in the v_F. With the pristine sample as a reference, the v_F variation as a function of the plasma power was computed from the a (see Table 1) and has also been plotted in the inset to Figure 3b. The initially lowered v_F was suggestive of positively charged defects/p-type doping due to the plasma processing.[28]

For obtaining the carrier concentrations to accommodate the partitioning into the various capacitances consistent with Eqns. (1)−(3), we numerically varied the n_{2D} (i.e., = $n_{2D,0}$) of the graphene layer closest to the electrolyte until the respective C_{SC} and C_Q were obtained and their sum in accordance with Eqn. (3) matched the C_{meas}. This involved for the C_Q in Eqn. (1) the net n_{2D} calculated using the summation of the carrier densities for all the FLG constituent layers, that is, Σ (l = 0, N, $n_{2D,l}$), where $n_{2D,l}$ is the carrier density in the lth layer, for the N + 1 layer FLG. In our experiments, N = 5. The $n_{2D,l} = n_{2D,0}\exp[-lx/\lambda_{TF}]$ with x being the distance between the layers of the FLG samples (see Section I.c and Figure S1 in the Supporting Information). The estimation of the λ_{TF} for Eqn. (2), also used an E_F (= $\hbar v_F(\pi n_{2D,0})^{1/2}$) − see Section I.b of the Supporting Information. The resultant variation of the series addition of the C_{SC} and the C_Q is indicated as C_{gr} and indicated in Figure 2b.

The estimated E_F, showed a close to 3-fold enhancement from ∼247 meV (for the pristine sample) to ∼661 meV (with 20 W plasma power). The underlying cause of an enhanced C_Q may then be ascribed to the decreasing E_F (in the negative sense, as would be the case for effective p-type doping) as schematically shown in Figure 3c. Generally, the effects of the Ar plasma treatment have been shown to be very reproducible, within the error bars represented by the data in Figure 2b. However, on further plasma processing (e.g., the 35 and 50 W cases), while the v_F appears to increase, the E_F diminishes. FLG fragmentation at such high powers, yielding negatively charged defects due to dominance of edge states, could be playing a role in such observations.[28,31]

Corresponding to the estimated $n_{2D,0}$, we defined a charge correlation length, $L_d = 1/(n_{2D,0})^{1/2}$, which may be understood as the average distance between charges (that could have arisen due to Ar^+ plasma induced defects) that contribute to the C_Q as well as the C_{SC}; also see Section II of the Supporting Information. Such a length scale should be compared to the more conventional Tuinstra−Koenig correlation length (L_a), discussed earlier in the context of Raman spectroscopy, where $A_D/A_G \sim 1/L_a$. In Figure 3d the respective variation of the L_d (right axis) and the L_a (left axis) as a function of the plasma power has been plotted. Note that the L_a is undefined for the pristine sample due to the negligible D-peak intensity; see Figure 1b. While a steady decrease of the L_a due to reduced crystallinity is expected, it was noted that (a) the L_d was typically smaller compared to the L_a, and (b) a definitive L_d may be prescribed even for the pristine sample. We further interpret L_d through the hypothesis that charged defects that contribute to electrochemical characteristics may not correspond to an effective crystallite size, considered through L_a. Instead, defects that are not diagnosed through Raman spectroscopy, e.g., ZZ edge states, may be relevant. An enhanced charged defect density would result in a lower L_d.

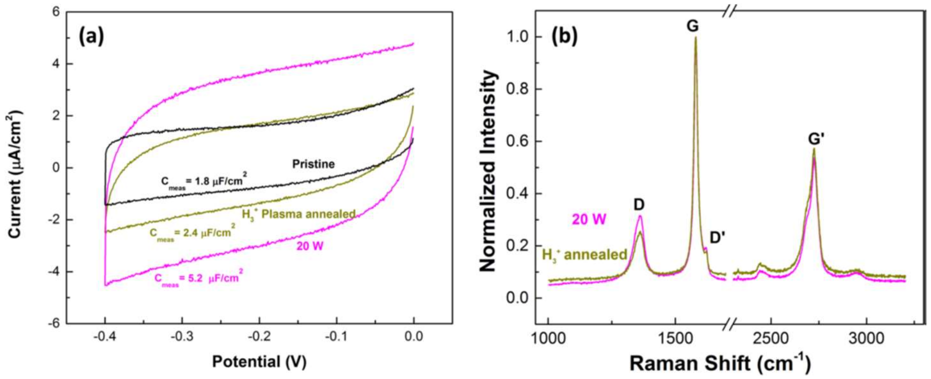

Figure 5-4. Tuning the capacitance of FLGs through hydrogen plasma treatment. (a) A pronounced 2-fold reduction of the capacitance was observed through CV characterization of H_3^+ ion plasma exposed plasma processed samples. Such observations validate the hypothesis that hydrogen passivates the charged defect sites and reduces the capacitance tending toward the pristine state. A residual capacitance on hydrogen exposure may indicate that there may be some residual defects that resist passivation. (b) The decrease in the FLG defect density on hydrogen ion exposure was manifested in the Raman spectra through a decreased A_D/A_G ratio and an increase in the L_a.

Having shown that the measured capacitance may be increased substantially through plasma processing, we now indicate further methodologies for the control of the net FLG capacitance. With such an aim, the argon plasma processed FLGs were subsequently subject to a hydrogen plasma, which had been shown[10] to be effective in passivating the number of dangling bonds and associated charged defect states. The influence of the charge contributing defects could then possibly be reduced with a concomitant decrease in the C_{meas}. In a typical hydrogen plasma,[32] there is a large variety of hydrogen ions, e.g., H^+, H_2^+, H_3^+, etc. and the processing conditions, mainly the gas pressure, must be regulated for the dominance of specific ions. Also, lower pressures may cause the hydrogen ions to induce additional defects.[10] Considering such factors, we used a hydrogen gas pressure of 1 Torr with H_3^+ as the predominant ion and obtained consistent and reproducible results. The hydrogen plasma power was set to be the same as that used for the initial Ar^+ plasma processing. The resultant lowering of the C_{meas} is indicated in Figure 4a and the concomitant Raman spectra are shown in Figure 4b. For the 20 W Ar+ plasma power processed sample, the H_3^+ plasma was effective in halving the capacitance and reduced the D-peak intensity as well. However, neither the C_{meas} nor the Raman intensity return to that noted for the pristine sample suggesting that (i) the hydrogen plasma may not be completely effective, or (ii) that there may be some residual defects that resist passivation. It was also noted through preliminary X-ray photoelectron spectroscopy (XPS) measurements (see Section III of the Supporting Information) that there was little evidence of the contribution of the surface functional groups, for example, quinones,[33] to the capacitance, as corroborated by a smooth CV scan; see Figure 2a.

In summary, we have indicated a methodology for both increasing and decreasing the electrochemical capacitance of FLG-based nanographites through a combination of argon and hydrogen-based plasma processing. In addition to the utility for charge storage, our work contributes to understanding and controlling the charge storage characteristics. The proposal of a new length scale, L_d, correlated to electrically active defects contributing to the capacitance, which is smaller than the conventional Tuinstra−Koenig correlation length determined through Raman spectroscopy, implies a distinction between electrical and structural length scales.

Acknowledgements

This work was supported by a grant (CMMI 1246800) from the National Science Foundation (NSF). We thank Dr. Matthew Baldwin of the Center for Energy Research (CER), UC, San Diego, profusely for the XPS measurements and help with the interpretation.

Chapter 5, in full, is a reprint of the material as it appears in R. Narayanan, H. Yamada, M. Karakaya, R. Podila, A. M. Rao, and P. R. Bandaru, Nano Lett. **15**, 3067-3072 (2015). The dissertation author was a co-author of this paper, and handled all of the theory and simulations.

References

[1] Kastnelson, M. I. Graphene: Carbon in Two Dimensions; Cambridge University press: Cambridge, U.K., 2012.

[2] Banhart, F.; Kotakoski, J.; Krasheninnikov, A. V. ACS Nano 2011, 5, 26.

[3] Stoller, M. D.; Park, S.; Zhu, Y.; An, J.; Ruoff, R. S. Nano Lett. 2008, 8, 3498.

[4] Simon, P.; Gogotsi, Y. Nat. Mater. 2008, 7, 845.

[5] Radic, S.; Geitner, N. K.; Podila, R.; Käkinen, A.; Chen, P.; Ke, P. C.; Ding, F. Sci. Rep. 2013, 3, 2273.

[6] Nichols, J. A.; Saito, H.; Deck, C.; Bandaru, P. R. J. Appled Phys. 2007, 102, 64306.

[7] Kelkar, U.; Gordon, M.; Roe, L.; Li, Y. J. Vac. Sci. Technol., A 1999, 17, 125.

[8] Zeng, J.-J.; Lin, Y.-J. Appl. Phys. Lett. 2014, 104, 233103.

[9] Lee, J.; Donohue, J. F.; Mackenzie, K. D.; Westerman, R.; Johnson, D.; Pearton, S. J. Solid-State Electron. 1999, 43, 1769.

[10] Hoefer, M.; Bandaru, P. R. J. Electrochem. Soc. 2013, 160, H360.

[11] Chen, P.; Fryling, M. A.; McCreery, R. L. Anal. Chem. 1995, 67, 3115.

[12] Malard, L.; Pimenta, M.; Dresselhaus, G.; Dresselhaus, M. Phys. Rep. 2009, 473, 51.

[13] Felten, A.; McManus, D.; Rice, C.; Nittler, L.; Pireaux, J.-J.; Casiraghi, C. Appl. Phys. Lett. 2014, 105, 183104.

[14] Knight, D. S.; White, W. B. J. Mater. Res. 1989, 4, 385.

[15] Tuinstra, F.; Koenig, J. L. J. Chem. Phys. 1970, 53, 1126.

[16] Pimenta, M. A.; Dresselhaus, G.; Dresselhaus, M. S.; Cançado, L. G.; Jorio, A.; Saito, R. Phys. Chem. Chem. Phys. 2007, 9, 1276.

[17] Rao, R.; Podila, R.; Tsuchikawa, R.; Katoch, J.; Tishler, D.; Rao, A. M.; Ishigami, M. ACS Nano 2011, 5, 1594.

[18] Cancado, L. G.; Pimenta, M. A.; Neves, B. R. A.; Dantas, M. S. S.; Jorio, A. Phys. Rev. Lett. 2004, 93, 247401.

[19] Nakada, K.; Fujita, M.; Dresselhaus, G.; Dresselhaus, M. Phys. Rev. B 1996, 54, 17954.

[20] Xia, J.; Chen, F.; Li, J.; Tao, N. Nat. Nanotechnol. 2009, 4, 505.

[21] Fang, T.; Konar, A.; Xing, H.; Jena, D. Appl. Phys. Lett. 2007, 91, 92109.

[22] Yamada, H.; Bandaru, P. R. Appl. Phys. Lett. 2013, 102, 173113.

[23] Gerischer, H. In The CRC Handbook of Solid State Electrochemistry; Gellings, P. J., Bouwmeester, H. J. M., Eds.; CRC Press: Boca Raton, FL, 1997.

[24] Ashcroft, N. W.; Mermin, N. D. Solid State Physics; Saunders College: Orlando, FL, 1976.

[25] Uesugi, E.; Goto, H.; Eguchi, R.; Fujiwara, A.; Kubozono, Y. Sci. Rep. 2013, 3, 1595.

[26] Bard, A. J.; Faulkner, L. R. Electrochemical Methods: Fundamentals and Applications, 2nd ed.; John Wiley: New York, 2001.

[27] Ashraf, A.; Wu, Y.; Wang, M. C.; Aluru, N. R.; Dastgheib, S. A.; Nam, S. Langmuir 2014, 30, 12827.

[28] Maciel, I. O.; Anderson, N.; Pimenta, M. A.; Hartschuh, A.; Qian, H.; Terrones, M.; Terrones, H.; Campos-Delgado, J.; Rao, A. M.; Novotny, L.; Jorio, A. Nat. Mater. 2008, 7, 878.

[29] Jorio, A.; Saito, R.; Dresselhaus, G.; Dresselhaus, M. S. Raman Spectroscopy in Graphene Related Systems; Wiley-VCH Verlag GmbH & Co. KGaA: Weinheim, 2011.

[30] Ferrari, A. C.; Meyer, J. C.; Scardaci, V.; Casiraghi, C.; Lazzeri, M.; Mauri, F.; Piscanec, S.; Jiang, D.; Novoselov, K. S.; Roth, S.; Geim, A. K. Phys. Rev. Lett. 2006, 97, 187401.

[31] Ferrari, A. C. Solid State Commun. 2007, 143, 47.

[32] Nunomura, S.; Kondo, M. J. Appl. Phys. 2007, 102, 93306.

[33] Okajima, K.; Ohta, K.; Sudoh, M. Electrochim. Acta 2005, 50, 2227.

[34] Podila, R.; Chacón-Torres, J.; Spear, J. T.; Pichler, T.; Ayala, P.; Rao, A. M. Appl. Phys. Lett. 2012, 101, 123108.

6. Dimensionality-dependent electrochemical kinetics at the single-layer graphene-electrolyte interface

The all-surface characteristic of single-layer graphene (SLG) offers a remarkable paradigm for the exploration of novel physical and chemical phenomena. However, many of the related observations, for example, the half-integer quantum Hall effect,[1] enhanced electrical and thermal conductivity[2] due to reduced phase space,[3,4] wrinkling,[5] and so forth are mostly concerned with electromechanical attributes, while the chemical aspects unique to graphene are less distinctive. For instance, in many cases, it is unclear as to how a graphene sheet manifests clearly different electrochemical character compared to any other surface.[6] Aspects related to hindered diffusion or selectivity may in many cases be attributed to the influence of defects[7] or the underlying substrate.[8] Here, we report on an electrochemical characteristic unique to the two-dimensional nature of SLG, adding another facet to interpreting reaction rates in terms of dependence on the dimensionality of charge transport.

SLG was synthesized via chemical vapor deposition (CVD) on copper foil and subsequently transferred to a SiO_2/p-Si substrate. The materials preparation related details have been previously reported[9] and are also discussed briefly in the Materials and Methods section of the Supporting Information. The transferred SLG films were first characterized through Raman spectroscopy (inset to Figure 1A), from which the single-layer aspect was verified[10] through the ratio of the intensities of the 2D- and the G-peak, that is, from an I_{2D}/I_G ratio of >2. The small D-peak intensity, that is, with an I_D/I_G ratio of ~0.05, is indicative[10,11] of the relatively high quality of the SLG. Surface structure characterization through atomic force microscopy reveals distinct wrinkles (Figure 1A) that have characteristic modulations on the order of 10 nm.

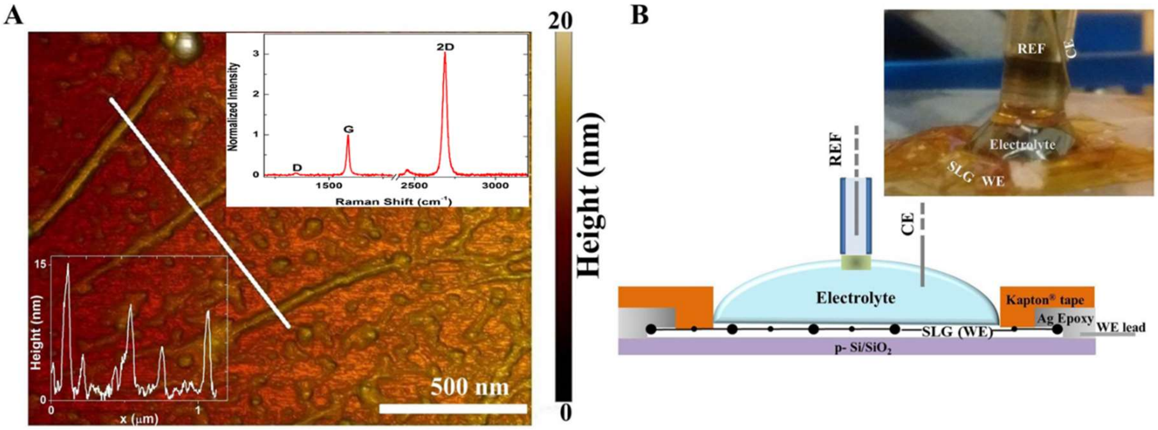

Figure 6-1. (A) Atomic force microscopy image of a section of the SLG sample transferred onto a p-Si/SiO2 substrate. The wrinkles on the sample surface corresponding to the line scan (white line) are displayed in the lower left inset. The Raman spectrum of the transferred SLG is indicated in the top right inset. (B) Schematic of the three-electrode droplet electrochemical cell (actual experimental arrangement shown in the top right inset). The SLG WE, Pt wire CE, and a REF saturated calomel electrode are indicated. Images courtesy of Rajaram Narayanan.

Electrochemical characterization of the SLG was performed using a three-electrode setup under potentiostatic control. An annular electrical contact (see the discussion in the Supporting Information related to Figures S1 and S2) using silver epoxy was used to surround the SLG surface, which served as the working electrode (WE), while a platinum wire and a saturated calomel electrode were used as the counter electrode (CE) and a standard calomel electrode-based reference electrode (REF), respectively, Figure 1B. The supporting electrolyte was an aqueous solution of 1 M KCl and was comprised of a 1 mM concentration (= C) redox couple, potassium ferri-/ferrocyanide, $K_3Fe(CN)_6^{3-}/K_4Fe(CN)_6^{4-}$, to study the specific reduction and oxidation reactions, respectively. A droplet (~100 μL) of electrolyte was cast onto the SLG over the area enclosed by the annular contact (silver epoxy). The contact was covered with Kapton tape to prevent exposure to electrolyte. We have ensured that the silver epoxy contacts do not have any influence on the observed results (see the discussion in the Supporting Information related to Figures S1, S2, S4, and S5, where the possible errors are considered in detail).

The reduction and oxidation of the electroactive moieties at the SLG electrode/electrolyte interface, considering the oxidizing species, O ($K_3Fe(CN)^{3-}$), and the reducing species, R ($K_3Fe(CN)_6^{4-}$), is represented through

$$O + e^- \leftrightharpoons R \ . \tag{1}$$

Here, k_f and k_b are the forward and backward heterogeneous reaction rate constants, respectively. Generally, k_f (/k_b) is proportional to the magnitude of the overpotential η (= V − V^{0}') with the applied potential V being negative (/positive) with respect to an equilibrium (formal) potential V^{0}'. Because at equilibrium the reaction in eq 1 must obey the Nernst relation,[12] we employ the relation $k_f/k_b = \theta$ (=exp [Fη/RT], with F (= 96 487 C/mol) as the Faraday constant and R (= 8.3 J/mol·K) as the gas constant at a given temperature T). At any given V, an overall reaction rate constant k = $k_f + k_b$ may also be defined. At equilibrium (i.e., at potential V^{0}'), $k_f = k_b = k_0$. It is to be noted that the k_f and k_b are the absolute values of the rate constants of electron transfer and are simultaneously operative at any stage of current flow (anodic/cathodic). We have consequently defined an overall rate constant, through $k = k_f + k_b$.

Cyclic voltammetry (CV) at a polished platinum electrode (of area 0.069 cm^2) was used to determine the V^{0}' of the $K_3Fe(CN)_6^{3-}$/$K_3Fe(CN)_6^{4-}$ redox couple (see the discussion in the Supporting Information related to Figure S3). Briefly, the potential (V) was scanned linearly with time within a potential window of 0.57 to −0.43 V (vs the standard calomel electrode reference) with a scan rate s in the range of 25−400 mV/s. The potential scan gives rise to a current response with peak currents associated with reduction ($i_{p\text{-}r}$) and oxidation ($i_{p\text{-}o}$) at potentials $V_{p\text{-}r}$ and $V_{p\text{-}o}$, respectively (see the discussion related to Figure S3A in the Supporting Information). The V^{0}' was taken to be the mean value of V_{p-r} and V_{p-o}. The redox reaction at the platinum electrode is considered reversible because the potential separation between the two peaks is ~59 mV at all s.[12] The relationship between $i_{p-r/o}$ and s (per the Randles−Ševčík equation, as discussed with reference to eq S1 and Figure S3A in the Supporting Information) was used to determine the diffusion coefficient of the O and R species, that is, $D_O = 6.21 \times 10^{-6}$ cm^2/s and $D_R = 6.77 \times 10^{-6}$ cm^2/s, respectively, in accord with previously reported values.[13] Typically, CV or the related Nicholson method[14–17] cannot be used to determine k_f ($/k_b$) because the current response beyond V_{p-r} ($/V_{p-o}$) (i.e., far from equilibrium) is mostly due to mass transport control (see the discussion after Figure S3 in the Supporting Information).

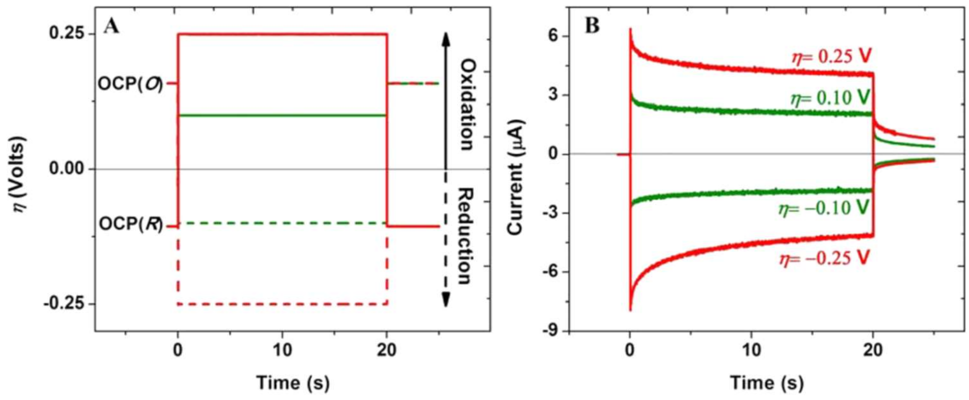

Figure 6-2. Chronoamperometry, involving (A) potential step experiments, was used to determine k_f and k_b. A potential step V with respect to the formal/equilibrium potential; $V^{0'}$ of the redox species, yielding an overpotential η (= $V - V^{0'}$), was applied for a time of 20 s with the electrode system initially at the open-circuit potential, V_{ocp}, for the oxidizing (O) and the reducing (R) species. (B) Varying η results in corresponding reduction (/oxidation) current transients, i(t), due to the combined influences of the diffusion-limited current as well as that due to the kinetics of electron transfer at the electrode/electrolyte interface, f (K).

Consequently, chronoamperometry (involving potential step experiments) was used to determine k_f and k_b at potentials far from equilibrium. Here, a potential step V was applied with respect to $V^{0'}$, for a time of 20 s (Figure 2A), with the electrode system initially at the open-circuit potential, V_{ocp}, at which there is no current flow. The application of a voltage (V) that is negative

(/positive) with respect to the $V^{0'}$ results in reduction (/oxidation) current transients, i(t) (Figure 2B), proportional to the magnitude of the η. The observed i(t) was parametrized[12] as due to the combined influences of the diffusion-limited current, i_D, as well as that due to the kinetics of electron transfer at the electrode/electrolyte interface through

$$i(t) = i_D f(K) \ . \tag{2}$$

Here, $i_D = \frac{nFAC_{O/R}\sqrt{D_{O/R}}}{\sqrt{\pi t}(1+\xi\theta)}$, and $f(K) = \sqrt{\pi}K \exp(K^2) \operatorname{erfc}(K)$, with $K = k_f\sqrt{\frac{t}{D_O}}(1+\xi\theta) = k_b\sqrt{\frac{t}{D_R}}\left(\frac{1+\xi\theta}{\xi\theta}\right)$.

The n is the number of transferred electrons, A (in cm^2) is the electrode area, CO/R (in mol/cm3) is the bulk concentration, $D_{O/R}$ is the diffusion coefficient of the O and R species in the electrolyte, ξ = sqrt(D_O/D_R), and erfc() is the complementary error function. The f (K) − t variation, as obtained by dividing i(t) by iD, from the experiments related to Figure 2B is plotted in Figure 3A. From this plot, the K and the involved rate constants, kf and kb, were deduced.

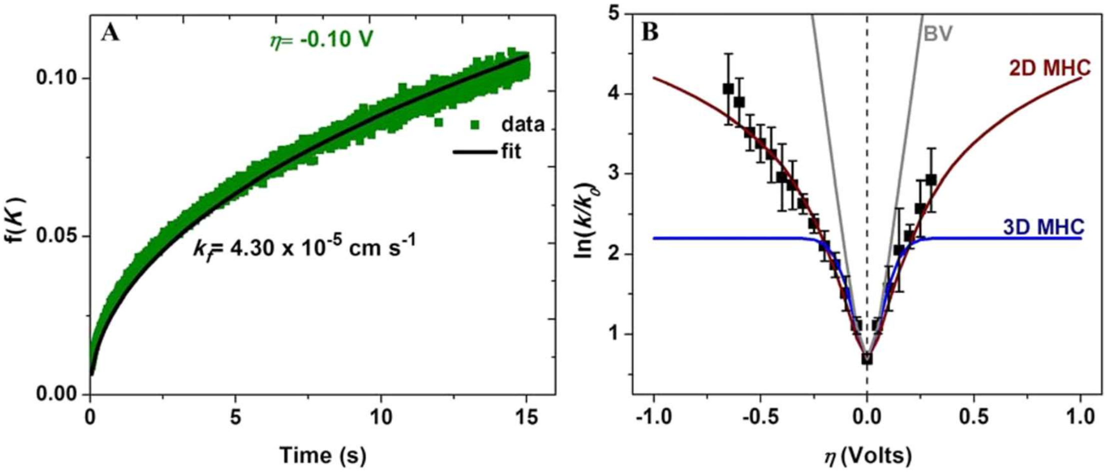

Figure 6-3. (A) The kinetics of electron transfer, parametrized through f(K) (see the text), was extracted from the i(t) data of Figure 2B. An instance of f(K) for the case of $\eta = -0.10$ V is shown. (B) Plot of the extracted rate constants ($k = k_f + k_b$, sum of the forward and the backward rate constants, respectively) normalized to the $k\eta$=0 V as a function of η. The experimental data is a poor fit with the theoretical fits expected from conventional B−V kinetics and three-dimensional MHC kinetics (blue MHC) assuming a constant DOS but could be modeled well through dimensionality-dependent electrochemical kinetics (red 2D DOS model), following Eqn. (3) in the text.

The overall rate constant k (= $k_f + k_b$), normalized to k_0 is plotted as a function of η in Figure 3b. It was immediately obvious that the observed $\ln(k/k_0) - \eta$ variation differs markedly from both Butler−Volmer (B−V) kinetics, where a linear relationship is expected on the semilog plot, as well as the Marcus−Hush[18-20]−Chidsey[21] (MHC) kinetics[22,23], which predicts a saturation of the rate constants with increased η. Alternatively, we observed for the SLG samples that while the slope monotonically decreases with increasing $|\eta|$ it never reaches zero within the stability limits of the electrolyte. We have also noted that the observed $\ln(k/k_0) - \eta$ variation cannot be fit by varying the series/film resistance.

We had earlier shown on theoretical grounds[24] that the specific consideration of the unusual two-dimensional density of states (DOS) of graphene stemming from the linear energy E-k relationship[3,4] would cause a deviation from Arrhenius activation based B−V kinetics and even the MHC kinetics. The assumption of the constant DOS, as in the MHC model, while appropriate for metals where the Fermi energy (E_F) is far above the bottom of the conduction band, does not hold for SLG. Instead, the linear variation of the DOS with energy, which is unique to two-dimensional graphene, must be considered. Consequently, a DOS-based reaction rate constant, k_{DOS}, is necessary, considering the influence of the discrete energy levels, through[24]

$$k^{DOS} = \nu k_B T \int_{-\infty}^{\infty} \frac{DOS\left|x+\frac{E_F-E_C}{k_BT}\right|}{1+\exp(x)} \exp\left(-\frac{k_BT}{4\lambda}\left[x-\frac{\lambda \pm e\eta}{k_BT}\right]^2\right) dx \ . \qquad (3)$$

In Eqn. (3), the integration is with respect to $x = (E-E_F)/k_BT$ and refers to the normalized energy of a relevant participating level E, for example, in the electrode, relative to the E_F. ν is the attempt frequency for the species undergoing redox reactions, k_B is the Boltzmann constant, and λ is the reorganization energy[23], which incorporates the energy required for both internal (e.g., due to the redox species' conformational changes) and external (e.g., involving rearrangement of the solvation shell with respect to the surrounding electrolyte and electrode related heterogeneous kinetics etc.) reaction coordinate changes[25]. The number of electrons available for the redox reaction is

$$n = \int_{E_C}^{\infty} f_{FD}(E-E_F)DOS(E-E_C)dE \ . \qquad (4)$$

Here, f_{FD} is the Fermi−Dirac distribution function, and E_C is the energy at the bottom of the conduction band. In a limiting case when the DOS is a constant, we revert to the original Chidsey formulation[21].

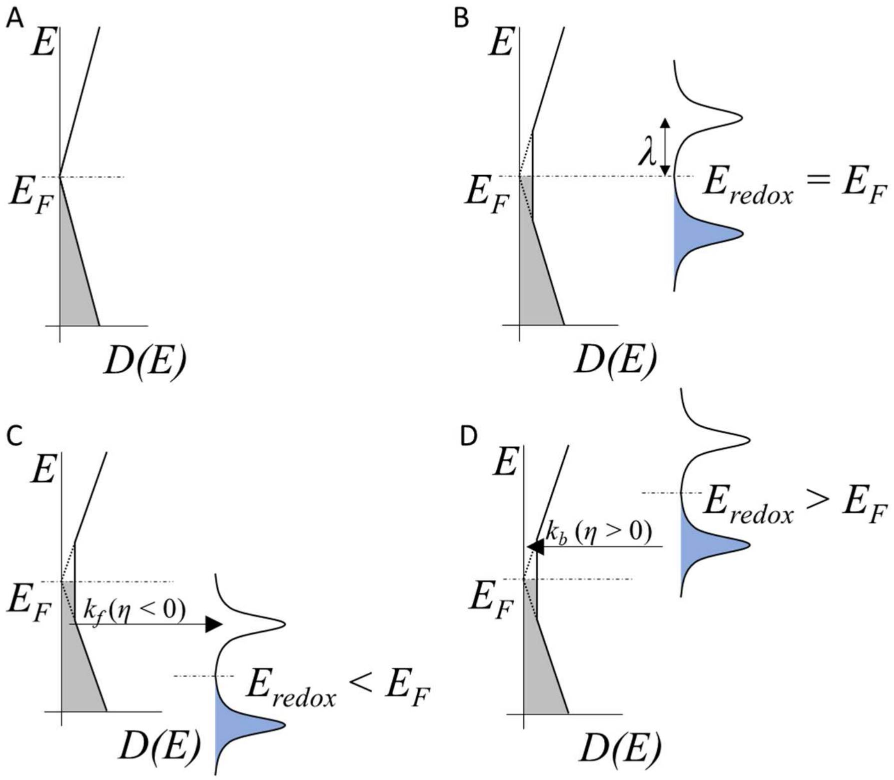

Figure 6-4. Schematic of (A) the energy (E) dependent density of states, DOS(E)/D(E), of an ideal SLG sheet. DOS(E) for a nonideal SLG (say, with wrinkles, electron, hole puddles, etc.), vis-a-vis the distribution functions of the O and R species in the redox couple, with respect to the overpotential (η) for (B) $\eta = 0$, (C) $\eta < 0$, and (D) $\eta > 0$, respectively. E_F and E_{redox} (= $eV^{0'}$) are the corresponding Fermi energy of the electrodes and the energy related to the formal/equilibrium potential, $V^{0'}$. The nonzero value of the DOS at the Dirac point is responsible for a finite electrochemical rate constant at $\eta = 0$, k_0.

Figure 4 is a schematic representation of the implications of Eqn. (3) for (b) $\eta = 0$, (c) $\eta < 0$, and (d) $\eta > 0$. Electron transfer from the electrode to electrolyte occurs from the filled carrier states in the electrode (following the Fermi−Dirac distribution) to the empty states in the electrolyte (which may be distributed in energy) following, for instance, a Gaussian distribution[26]. With varying η, the electrolyte states effectively scan over the DOS distribution of the electrode, implying that the k/k_0 variation mimics the electrode DOS. For a pristine graphene sheet (e.g., defect or wrinkle free), $n = 0$ at the Dirac point, and it would be expected that $k_0 = 0$. However, a finite value for k_0 with the implication of a nonzero DOS was observed. We then fit the experimental data (depicted through the "2D DOS model" in Figure 3b) assuming a finite and constant DOS close to $\eta = 0$ and found that the energy width of such a constant DOS region could be at most 2λ. A best fit, with a width of 2λ where $\lambda = 4k_BT$ (~104 meV at room temperature) is indicated in Figure 3b. Beyond $e\eta \approx \pm\lambda$, the linear variation of the DOS resumes, yielding an increasing k/k_0 with η.

Physically, the source of this additional, nonideal DOS variation could be due to the formation of both[27] electron and hole puddles as well as inevitably induced wrinkles[28,29], as in Figure 1a. Up to a threshold $|\eta| = 4k_BT \approx 104$ meV, corresponding to the constant DOS near the Dirac point, increasing (/decreasing) η would only result in reducing electron (/hole) puddle concentrations that seem to be present in equal numbers as deduced from the symmetry of the data in Figure 3b. Only beyond a threshold $|\eta|$ would the DOS increase linearly, concomitant with an increase of the carrier concentration and resulting Fermi energy. Assuming that each electron/hole puddle has a sufficient number of carriers to yield concomitant quasi-Fermi levels of ±104 meV, we estimated, from Eqn. (4), an intrinsic puddle carrier concentration of $\sim 8 \times 10^{11}$ cm^{-2}, which is plausible for undoped graphene on the substrate; previous work[30,31] on graphene in electrochemical cells has shown such intrinsic doping[32] of up to 10^{12} cm^{-2}.

The small deviation of the fit from the experimental data, at increasingly negative η, that is, say, less than -0.6 V, could be due to both (i) theoretical assumptions as well as (ii) experimental causes. First, a linear variation with energy of the DOS of graphene, based on the typically assumed linear energy E−k relationship, was considered. However, there would be a deviation from linearity[3,4] (due to a reduced dE/dk yielding an increased DOS) at increasing $|\eta|$, especially when electron transfer takes place from deeper occupied energy levels in the graphene to the electrolyte. Consequently, the DOS of a realistic graphene sample must be considered at increasingly negative

η and would push the fit to higher values. Alternately, background hydrogen evolution (from aq. KCl) could also contribute to the derived rate constants. Experiments in aprotic solvents may yield more reliable rate constants.

Our experiments and related fitting of the experimental data through a DOS-based reaction rate constant considerably add to the presently used standard models to analyze the variation of the $(k/k_0)-\eta$ data, which predict that for $e|\eta|$ greater than the λ the k/k_0 would tend to a constant value. In this regard, such MHC-based models, while seemingly appropriate for most macroscale metallic electrodes, need correction[33] for nanoscale electrodes such as graphene. We have seen in Figure 2B that the obtained data on the SLG cannot be fit with extant Marcus−Hush theory (Figure S6 in the Supporting Information) or MHC kinetics (Figure S7 in the Supporting Information). Consequently, our work also bares open intriguing aspects related to the necessity for a deeper theoretical and experimental investigation[34] of dimensionality-related effects in electrochemical kinetics. The implications of our study extend to properly modeling the electrical current that could be obtained in electrochemical and biological systems, with applications incorporating battery-related systems, wearable sensors, and so forth.

Acknowledgements

The authors are grateful for support from the Defense Advanced Research Projects Agency (DARPA: W911NF-15- 2-0122) and the National Science Foundation (NSF: CMMI 1246800 and CBET 1606192). The assistance of Prof. D. Lipomi and discussions with Prof. P. Asbeck are appreciated.

Chapter 6, in full, is a reprint of the material as it appears in R. Narayanan, H. Yamada, B. C. Marin, A. Zaretski, and P. R. Bandaru, J. Phys. Chem. Lett. **8**, 4004-4008 (2017). The dissertation author was a co-author of this paper, and handled all of the theory and simulations.

References

[1] Zhang, Y.; Tan, Y.-W.; Stormer, H. L.; Kim, P. Experimental Observation of the Quantum Hall Effect and Berry's Phase in Graphene. Nature 2005, 438, 201−204.

[2] Nika, D. L.; Balandin, A. A. Two-Dimensional Phonon Transport in Graphene. J. Phys.: Condens. Matter 2012, 24, 233203.

[3] Castro Neto, A. H.; Guinea, F.; Peres, N. M. R.; Novoselov, K. S.; Geim, A. K. The Electronic Properties of Graphene. Rev. Mod. Phys. 2009, 81 (1), 109−162.

[4] Das Sarma, S.; Adam, S.; Hwang, E. H.; Rossi, E. Electronic Transport in Two-Dimensional Graphene. Rev. Mod. Phys. 2011, 83, 407.

[5] Geim, A. K.; Novoselov, K. S. The Rise of Graphene. Nat. Mater. 2007, 6 (3), 183−191.

[6] Ambrosi, A.; Chua, C. K.; Bonanni, A.; Pumera, M. Electrochemistry of Graphene and Related Materials. Chem. Rev. 2014, 114, 7150−7188.

[7] Yao, F.; Güneş, F.; Ta, H. Q.; Lee, S. M.; Chae, S. J.; Sheem, K. Y.; Cojocaru, C. S.; Xie, S. S.; Lee, Y. H. Diffusion Mechanism of Lithium Ion through Basal Plane of Layered Graphene. J. Am. Chem. Soc. 2012, 134 (20), 8646−8654.

[8] Diankov, G.; Neumann, M.; Goldhaber-Gordon, D. Extreme Monolayer-Selectivity of Hydrogen-Plasma Reactions with Graphene. ACS Nano 2013, 7 (2), 1324−1332.

[9] Zaretski, A. V.; Moetazedi, H.; Kong, C.; Sawyer, E. J.; Savagatrup, S.; Valle, E.; O'Connor, T. F.; Printz, A. D.; Lipomi, D. J. Metal-Assisted Exfoliation (MAE): Green, Roll-to-Roll Compatible Method for Transferring Graphene to Flexible Substrates. Nanotechnology 2015, 26 (4), 045301.

[10] Beams, R.; Gustavo Cancado, L.; Novotny, L. Raman Characterization of Defects and Dopants in Graphene. J. Phys.: Condens. Matter 2015, 27 (8), 083002.

[11] Narayanan, R.; Yamada, H.; Karakaya, M.; Podila, R.; Rao, A. M.; Bandaru, P. R. Modulation of the Electrostatic and Quantum Capacitances of Few Layered Graphenes through Plasma Processing. Nano Lett. 2015, 15 (5), 3067−3072.

[12] Bard, A. J.; Faulkner, L. R. Electrochemical Methods: Fundamentals and Applications, 2nd ed.; 2001.

[13] Compton, R. G.; Banks, C. E. Understanding Voltammetry; Imperial College Press: London, U.K., 2011.

[14] Bard, A. J.; Faulkner, L. R. Electrochemical Methods: Fundamentals and Applications, 2nd ed.; John Wiley: New York, 2001.

[15] Toth, P. S.; Valota, A. T.; Velicky, M.; Kinloch, I. A.; Novoselov, K. S.; Hill, E. W.; Dryfe, R. A. W. Electrochemistry in a Drop: A Study of the Electrochemical Behavior of Mechanically Exfoliated Graphene on Photoresist Coated Silicon Substrate. Chem. Sci. 2014, 5, 582−589.

[16] Velicky, M.; Bradley, D. F.; Cooper, A. J.; Hill, E. W.; Kinloch, I. A.; Mishchenko, A.; Novoselov, K. S.; PAtten, H. V.; Toth, P. S.; Valota, A. T.; et al. Electron Transfer Kinetics on Mono-and Multilayer Graphene. ACS Nano 2014, 8, 10089−10100.

[17] Valota, A. T.; Kinloch, I. A.; Novoselov, K. S.; Casiraghi, C.; Eckmann, A.; Hill, E. W.; Dryfe, R. A. W. Electrochemical Behavior of Monolayer and Bilayer Graphene. ACS Nano 2011, 5, 8809−8815.

[18] Marcus, R. A. Theoretical Relations among Rate Constants, Barriers, and Broensted Slopes of Chemical Reactions. J. Phys. Chem. 1968, 72 (3), 891−899.

[19] Marcus, R. A. Electron Transfer Reactions in Chemistry: Theory and Experiment. Rev. Mod. Phys. 1993, 65, 599.

[20] Hush, N. S. Electron Transfer in Retrospect and Prospect 1: Adiabatic Electrode Processes. J. Electroanal. Chem. 1999, 470 (2), 170−195.

[21] Chidsey, C. E. Free Energy and Temperature Dependence of Electron Transfer at the Metal-Electrolyte Interface. Science 1991, 251 (4996), 919−922.

[22] Henstridge, M. C.; Laborda, E.; Rees, N. V.; Compton, R. G. Marcus−Hush−Chidsey Theory of Electron Transfer Applied to Voltammetry: A Review. Electrochim. Acta 2012, 84, 12−20.

[23] Henstridge, M. C.; Batchelor-McAuley, C.; Gusmão, R.; Compton, R. G. Marcus−Hush−Chidsey Theory of Electron Transfer to and from Species Bound at a Non-Uniform Electrode Surface: Theory and Experiment. Chem. Phys. Lett. 2011, 517 (1−3), 108−112.

[24] Yamada, H.; Bandaru, P. R. Electrochemical Kinetics and Dimensional Considerations, at the Nanoscale. AIP Adv. 2016, 6 (6), 065325.

[25] Fletcher, S. The Theory of Electron Transfer. J. Solid State Electrochem. 2010, 14, 705−739.

[26] Gerischer, H. Principles of Electrochemistry. In The CRC Handbook of Solid State Electrochemistry; Gellings, P. J., Bouwmeester, H. J. M., Eds.; CRC Press: Boca Raton, FL, 1997.

[27] Martin, J.; Akerman, N.; Ulbricht, G.; Lohmann, T.; Smet, J. H.; von Klitzing, K.; Yacoby, A. Observation of Electron−hole Puddles in Graphene Using a Scanning Single-Electron Transistor. Nat. Phys. 2008, 4 (2), 144−148.

[28] Pereira, V. M.; Castro Neto, A. H.; Liang, H. Y.; Mahadevan, L. Geometry, Mechanics, and Electronics of Singular Structures and Wrinkles in Graphene. Phys. Rev. Lett. 2010, 105 (15), 156603.

[29] Zhu, W.; Low, T.; Perebeinos, V.; Bol, A. A.; Zhu, Y.; Yan, H.; Tersoff, J.; Avouris, P. Structure and Electronic Transport in Graphene Wrinkles. Nano Lett. 2012, 12 (7), 3431−3436.

[30] Chen, J.-H.; Jang, C.; Xiao, S.; Ishigami, M.; Fuhrer, M. S. Intrinsic and Extrinsic Performance Limits of Graphene Devices on SiO2. Nat. Nanotechnol. 2008, 3 (4), 206−209.

[31] Akturk, A.; Goldsman, N. Electron Transport and Full-Band Electron-Phonon Interactions in Graphene. J. Appl. Phys. 2008, 103 (5), 053702.

[32] Xia, J.; Chen, F.; Li, J.; Tao, N. Measurement of the Quantum Capacitance of Graphene. Nat. Nanotechnol. 2009, 4, 505−509.

[33] Bai, P.; Bazant, M. Z. Charge Transfer Kinetics at the Solid- Solid Interface in Porous Electrodes. Nat. Commun. 2014, 5, 3585.

[34] Park, B. Y.; Zaouk, R.; Wang, C.; Madou, M. J. A Case for Fractal Electrodes in Electrochemical Applications. J. Electrochem. Soc. 2007, 154, P1−P5.

CONCLUSION

The ideal electrochemical cell has both a large capacitance (large total energy) and a high current output (high power output). First, regarding electrons in the nanoscale electrode, we want a large capacitance. However, the strong localization of nanostructures causes quantum capacitance to be small enough to affect the series-connected total capacitance of the device. Second, regarding ions in the electrolyte, we want a large device current. To achieve higher current, a longer screening length is desirable, which is determined by how easily ions can move in response to an electric field. Third, regarding charge transfer between electrons and ions across the solid-liquid boundary, we again want a large device current. The electrons carrying this current must have both a starting point and an ending point, i.e. sufficient filled states in electrode and sufficient empty states in electrolyte ions, or vice versa. I hope this serves as an original framework for further understanding of the electrochemical cell.